The Astrophysical Journal, 935:92 (22pp), 2022 August 20 https://doi.org/10.3847/1538-4357/ac7e50

The Physical Properties of Low-redshift FeLoBAL Quasars. II. The Rest-frame Optical Emission Line Properties

Karen M. Leighly[1], Hyunseop Choi[1], Cora DeFrancesco[1], Julianna Voelker[1], Donald M. Terndrup[1,2], Sarah C. Gallagher[3,4,5,6], and Gordon T. Richards[7]

[1] Homer L. Dodge Department of Physics and Astronomy, The University of Oklahoma, 440 W. Brooks St., Norman, OK 73019, USA; leighly@ou.edu
[2] Department of Astronomy, The Ohio State University, 140 W. 18th Ave., Columbus, OH 43210, USA
[3] Department of Physics & Astronomy, The University of Western Ontario, London, ON, N6A 3K7, Canada
[4] Canadian Space Agency, 6767 Route de l'Aéroport, Saint-Hubert, QC, J3Y BY9, Canada
[5] Institute for Earth and Space Exploration, The University of Western Ontario, London, ON, N6A 3K7, Canada
[6] The Rotman Institute of Philosophy, The University of Western Ontario, London, ON, N6A 3K7, Canada
[7] Department of Physics, Drexel University, 32 S. 32nd St., Philadelphia, PA 19104, USA

Received 2021 December 16; revised 2022 June 26; accepted 2022 June 30; published 2022 August 19

Abstract

We report the results of an analysis of the Hβ emission line region of a sample of 30 low-redshift ($z < 1$) iron low-ionization broad absorption line quasars (FeLoBALQs). Eleven of these objects are newly classified as FeLoBALQs. A matched sample of 132 unabsorbed quasars was analyzed in parallel. The emission lines showed the well-known anticorrelation between the [O III] and Fe II emission. Using a summary statistic called $E1$ to quantify this anticorrelation, we found that while the distribution of $E1$ for the unabsorbed quasars has a single peak, the FeLoBALQs have a bimodal shape in this parameter. Previous studies have shown that the line emission properties of BAL and non-BALQs are consistent; therefore, the difference in the Hβ region emission between FeLoBALQs and unabsorbed quasars is a new result. The two populations of FeLoBALQs are characterized by low and high bolometric luminosities and Eddington ratios. Some previous studies have suggested that BALQs are high accretion rate objects and therefore the discovery of the low accretion rate branch of FeLoBAL quasars was unexpected. We also found that the Hβ FWHM is systematically broader among the FeLoBALQs, implying a higher inclination viewing angle or a dearth of low velocity line emitting gas.

Unified Astronomy Thesaurus concepts: Broad-absorption line quasar (183); Quasars (1319)

Supporting material: figure set

1. Introduction

Broad absorption lines occur in 10%–26% of optically selected quasars (Tolea et al. 2002; Hewett & Foltz 2003; Reichard et al. 2003; Trump et al. 2006; Knigge et al. 2008; Gibson et al. 2009). The broad and blueshifted C IV absorption lines observed in broad absorption line quasars (BALQs) reveal an unambiguous signature of outflow. Therefore, BALQs may be important sources of quasar feedback in galaxy evolution. Trump et al. (2006) found that 1.3% of quasars have broad Mg II absorption; these are called low-ionization broad absorption line quasars (LoBALQs). A typical median width of a LoBALQ Mg II broad absorption line is 4400 km s^{-1} (Yi et al. 2019). Trump et al. (2006) found that 0.3% of quasars also have absorption from Fe II, and these are called iron low-ionization broad absorption line quasars (FeLoBALQs). FeLoBALQs are rare, and, prior to the Sloan Digital Sky Survey (SDSS), only a few were known. For example, Hall et al. (2002) published spectra and discussed the wide range of features observed in 23 unusual objects discovered in the SDSS; many of those objects are FeLoBALQs.

How do BALQs, and FeLoBALQs specifically, fit in among quasars in general? Are they fundamentally the same, and their magnificent spectra are observed because of a select range of viewing angles? Or do they mark a special stage in quasar evolution? Or are both factors important?

One way to address these questions is to look at the broad emission lines. Weymann et al. (1991) performed the first comprehensive study of the emission line properties of BAL and unabsorbed quasars, focusing on the rest-frame UV emission lines observed in ground-based spectra. They found that, with the exception of LoBALQs, the line emission was indistinguishable from that of unabsorbed quasars. This result makes sense if the emission lines in both types of objects originate in a similarly photoionized broad-line region (rather than, e.g., an expanding outflow like a supernova). Modern studies using larger samples have found a somewhat different pattern of behaviors that link the outflow properties with the emission line and continuum properties. For example, Baskin et al. (2015) reported that the He II λ1640 equivalent width is inversely related to the velocity shift and width of the BAL absorption. This result has been confirmed by further analysis (Hamann et al. 2019; Rankine et al. 2020). Because weak He II is a signature of a UV-dominant or soft spectral energy distribution (SED; e.g., Leighly 2004), these results may imply that the illuminating SED in at least some BALQs tends to be soft.

The rest-frame optical bandpass is arguably the best-studied region of quasar spectra, containing the Hβ, [O III], and Fe II lines that are routinely used to measure black hole masses and Eddington ratios. The rest-frame optical band has been less well studied in BALQs than the rest-frame UV band because this band is observed in the near-infrared when C IV λ1549 is observed in the optical band. Yuan & Wills (2003) reported results from 16 BALQs and a comparison sample of 13 non-BALQs. They found that the [O III] lines are weak in BALQs. Runnoe et al. (2013) reported results from a sample of eight moderate-redshift radio-loud BALQs. They also found weak [O III] and strong Fe II in these objects, suggesting a high accretion rate (e.g., Boroson 2002; Shen & Ho 2014). However, analysis of the Balmer line widths and estimation of the black hole masses revealed the Eddington ratios that were consistent with comparable unabsorbed quasars. Schulze et al. (2017) presented the largest sample of LoBALQs and FeLoBALQs studied in the rest-frame optical band, with near-IR spectroscopy from 16 LoBALQs and six FeLoBALQs. Sixteen of the spectra cover the Hβ/[O III] region. Their results deviate from the previous work; they saw neither notably weak [O III] nor notably strong Fe II emission. Instead, they found that their $z \sim 1.5$ subsample composite spectrum may have weaker Fe II emission than the unabsorbed quasars.

These three studies of the rest-frame optical spectra of BALQs leave the impression that BALQs often appear to be high Eddington ratio objects. More recently, Rankine et al. (2020) estimated the Eddington ratio in BALQs using a reconstructed C IV emission line and a profile correction (Coatman et al. 2017). They found that the Eddington ratio distribution is indistinguishable between BALQs and unabsorbed quasars.

A complicating factor is the luminosity of the objects studied. Many quasar properties are luminosity-dependent (e.g., the Baldwin effect; Baldwin 1977). The BAL outflow velocities are observed to have a particularly strong dependence on quasar luminosity (e.g., Laor & Brandt 2002; Ganguly et al. 2007). This dependence may be expected; for a fixed $L_{\rm Bol}/L_{\rm Edd}$, a more luminous black hole will have a larger black hole mass. That larger black hole mass yields an SED that peaks at longer wavelengths. This softer SED may influence the outflows in two ways. (1) Soft SEDs are less likely to overionize the outflowing gas. (2) The soft SED produces a relatively higher flux density of the UV photons responsible for accelerating the outflow via resonance line driving. Quasar luminosity evolution and flux-limited surveys combine to yield higher-luminosity objects at larger redshifts (Jester et al. 2005). It is therefore not clear that samples of objects with different redshifts and luminosities can be compared directly.

This paper is the second in a series of four papers. Choi et al. (2022, hereafter Paper I) described the SimBAL (Leighly et al. 2018) spectral synthesis analysis of the BAL outflows in 50 low-redshift FeLoBALQs. In this paper, Paper II, we present an analysis of the rest-frame optical-band spectra of a subsample of 30 of the 50 FeLoBALQs considered in Choi et al. (2022). All of the objects in this subsample have redshifts $z < 1$, and the SDSS/BOSS spectra include the Hβ/[O III] region of the spectrum. Paper III (H. Choi et al. in preparation) combines the SimBAL results from Paper I and the emission line analysis of this paper to discuss the implications for the location and geometry of the outflow. Paper IV (K. M. Leighly et al. 2022, in preparation) includes the broadband optical/IR properties and discusses the potential implications for accretion models and evolution scenarios for low-redshift FeLoBALQs.

Our paper is organized as follows. In Section 2, we describe the data selection of the FeLoBALQs and a matched comparison sample of 132 unabsorbed quasars, the optical-band modeling, and a principal component analysis of the spectrum around Hβ. In Section 3, we compare the optical and derived properties of the FeLoBALQs with those of the comparison sample. We present our reasoning and methodology for dividing the FeLoBALQs into two groups. We also look at correlations and patterns among the emission line and global properties and compare with previous results from the literature. Section 4 summarizes our results.

2. Data

2.1. Sample Selection

The parent sample of the FeLoBALQs was drawn from three sources: the literature, from the sample of $0.8 < z < 3.0$ FeLoBALQ candidates that were found in the DR14 quasar catalog (Pâris et al. 2018) using a convolutional neural net trained with synthetic spectra (Dabbieri et al. 2020; C. Dabbieri et al. 2022, in preparation), and from visual inspection. The redshift range of the objects was principally between ~0.7 and 1.0; several of the objects with redshifts smaller than $z = 0.75$ are well-known FeLoBALQs (FBQS J104459.5+365605, FBQS J1214+2803; de Kool et al. 2001, 2002). The resulting sample included 30 objects that had spectra of sufficient quality to analyze both the BAL absorption at the short-wavelength end and the Hβ and [O III] emission at the long-wavelength end. The other 20 objects analyzed by Choi et al. (2022) had too high redshift to include the rest-frame Hβ and [O III] emission at the long-wavelength end. The spectra of five example FeLoBALQs from the sample displayed in Figure 1 illustrate the wide range of absorption and emission line properties in the sample. The properties of the sample are presented in Table 1 of Choi et al. (2022).

The sample of 30 objects can be divided into three classes depending on the origin of their BAL classification. Ten objects are classified as BALQs in the NASA/IPAC Extragalactic Database (NED).[8] Nine more are included in the SDSS DR12 BALQ catalog (Pâris et al. 2017). The remaining 11 are newly classified as BALQs.

For comparison, we created a sample of unabsorbed quasars. Our goal was to identify five unabsorbed quasars from the SDSS DR14 (Pâris et al. 2018) for each FeLoBALQ. For each FeLoBALQ, we selected a set of unabsorbed objects that lay near it in redshift, 3 μm luminosity density, and signal-to-noise ratio (S/N). Our criteria for proximity were $\Delta \log F_{3\mu} = 0.3$, $\Delta z = 0.01$, and ΔS/N$= 0.1$. Many quasar properties depend on luminosity; examples include the emission line equivalent widths (Baldwin 1977) and BAL velocity (e.g., Ganguly et al. 2007). BALQs tend to be reddened (e.g., Krawczyk et al. 2015), and evidence for reddening is present in this sample (Leighly et al. 2022, in preparation). Therefore, we use the 3 μm luminosity as representative, rather than the luminosity in the optical or UV. From those, we randomly chose five objects, visually inspecting each one to be sure that it was not a BALQ and had analyzable Hβ/[O III] emission lines; i.e., the Hβ line could be discerned by eye. Six objects had such high S/Ns that this selection method yielded too few comparison objects. For those, the redshift criterion was relaxed. Finally, the three objects with the poorest S/Ns did not yield a sufficient analyzable comparison sample; regardless, we retained these objects in our FeLoBALQ sample. The result was a comparison

---

[8] http://ned.ipac.caltech.edu

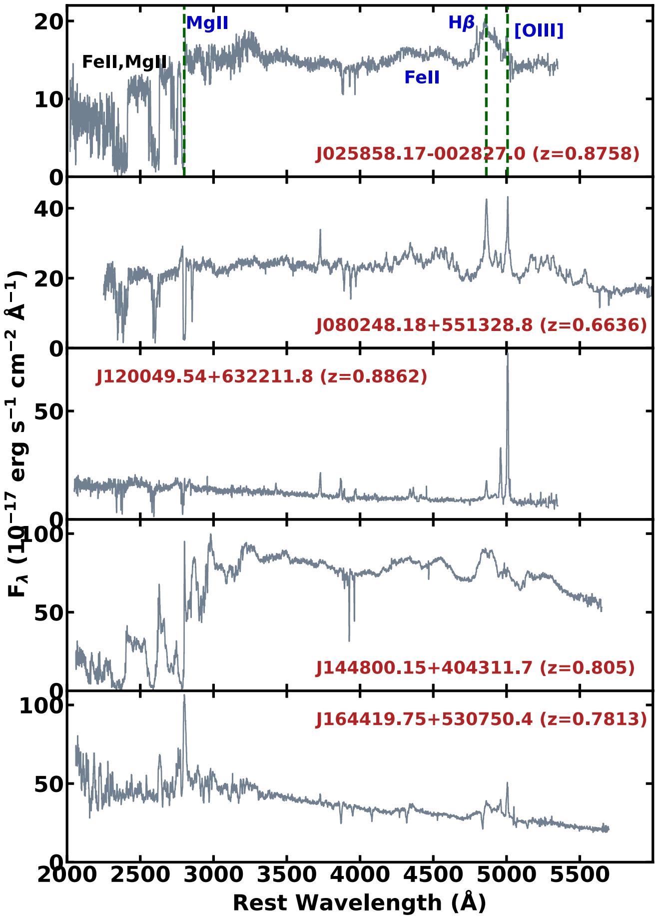

Figure 1. The SDSS or BOSS spectra of five FeLoBALQs from our sample. The Fe II and Mg II absorption can be seen at short wavelengths, and the Hβ, [O III], and Fe II complex is present at long wavelengths. The vertical dashed lines in the top panel show the rest-frame wavelengths of Mg II, Hβ, and the 5007 Å component of [O III]. A wide range of absorption and emission morphologies can be seen. The optical-band spectra of the full sample are shown in Figure 3, while the near-UV spectra (with SimBAL model fits) are found in Choi et al. (2022).

sample of 132 unabsorbed quasars. The distribution of the sample properties is shown in Figure 2.

2.2. Optical-band Modeling

Our goals for the optical-band modeling were to fine-tune the redshifts (necessary to measure the outflow velocities), extract the Hβ properties to estimate the black hole mass, and extract the [O III] and Fe II properties. We modeled the optical-band spectra using `Sherpa`[9] (Freeman et al. 2001). Although intended for spectral fitting in the X-ray band, `Sherpa` has more than sufficient flexibility and robustness to fit optical spectra.

In order to take into account the potential covariance between the emission lines, continuum, and Fe II pseudocontinuum, we modeled all components simultaneously. Most of the spectra were modeled between 3550 and 5500 Å. Some Seyfert 1.5 and 1.8 objects were modeled down to 3300 to include the [Ne V] lines. Sometimes the long-wavelength limit was as low as 5200 Å for higher-redshift objects due to the long-wavelength limit of the SDSS/BOSS spectrograph.

Estimating the redshift from optical emission lines is known to be difficult because many lines show evidence for outflows. Following the discussion in Zakamska & Greene (2014), we usually used the lowest-ionization narrow line available to estimate the redshift. When narrow Hβ could be clearly distinguished from broad Hβ, we used that; narrow Hβ was fit in 16 out of 30 of the spectra. Most commonly, we used [O II] λ3727, which was present in 27 out of 30 of the spectra. The [O II] emission was fit with two lines with line widths constrained to be equal and equal intensities. More correctly, the intensities should be constrained to be 1:5.5 (Osterbrock & Ferland 2006), resulting in a shift of 0.97 Å of the centroid, an amount that is comparable to the spectral resolution. Thus, the redshifts estimated using the [O II] line are high by $\Delta z = 0.00026$. Considering the uncertainty in the redshift estimation of SDSS active galactic nucleus (AGN) spectra in general (e.g., Zakamska & Greene 2014), and the fact that it could not affect the results of the paper, this error was deemed to be unimportant. When neither line was available, the SDSS DR14 redshift was used, or the redshift was estimated from the shape of the near-UV Fe II emission.

The continuum under the Hβ and [O III] lines was modeled using a power law. In some cases, we observed an upturn of the spectrum toward shorter wavelengths. We modeled that upturn with either a recombination continuum model or a broken power-law model.

Most frequently, we modeled the Fe II emission using the line lists developed from the strong Fe II Seyfert galaxy I Zw 1 (Véron-Cetty et al. 2004). In a few cases, the Fe II emission is very prominent and complex, and we used the more flexible Fe II model constructed by Kovačević et al. (2010). This model is comprised of five line lists, three of which correspond to different lower levels of the transitions. This model only spans 4400–5500 Å, and we modeled the 3550–4400 Å region using the Véron-Cetty et al. (2004) model, fitting both segments of the spectrum simultaneously.

The Balmer lines (Hβ, Hγ, Hδ, and Hϵ) were modeled using either a single Lorentzian profile, a single Gaussian profile, or two Gaussians. When a cusp could be seen in the Hβ profile, the broad lines were modeled with Gaussians, and a set of narrow Gaussian lines were included to model the narrow Balmer emission. There should be a contribution to the Hβ profile from the narrow-line region, but we did not model it unless a cusp was present. We experimented with including a narrow Hβ component with width and position tied to the [O III] lines and an intensity of one-tenth of the [O III] emission (Cohen 1983) and found that the measurements of Hβ agreed within the error bars with the results of models that did not include a scaled narrow component. The two-broad-Gaussians profile was only required for a few objects and most frequently used when the Hβ line appeared to have a red wing.

We modeled the [O III] lines with either one or two pairs of Gaussian profiles. As usual, the 5007Å component was constrained to have the same width, 2.92 times the intensity, and lie a fixed wavelength ratio from the 4959 Å component. In most cases, the preferred model used two pairs of lines; however, one pair was used when the line was particularly weak (especially when Fe II was strong).

Several objects (J1030+3120, J1044+3656, J1214+2803, and J1448+4043) were particularly challenging to model because of a combination of a good S/N, strong Fe II, and weak [O III]. One of the complicating factors is that we

---

[9] https://sherpa.readthedocs.io/en/latest/

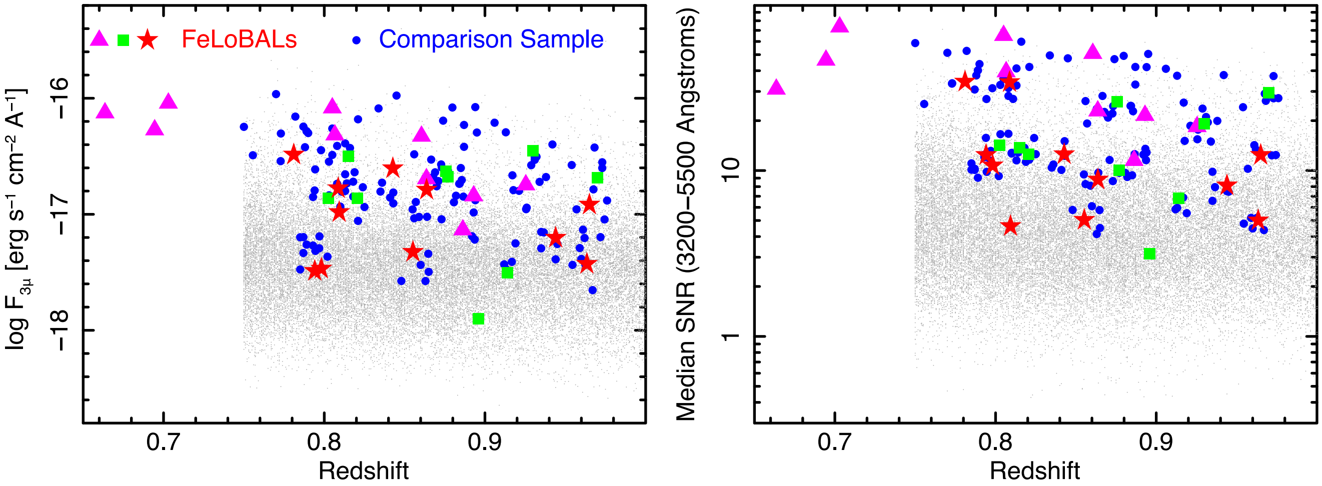

Figure 2. Distribution of the FeLoBALQ and comparison sample as a function of the comparison sample matching properties: the 3 μm flux density, redshift, and median S/N in the rest-frame 3200–5500 Å bandpass. The FeLoBALQs are subdivided into objects classified as BALQs in NED (magenta triangles), included in the SDSS DR12 BAL catalog (green squares; Pâris et al. 2017), and newly classified as BALQs (red stars). The redshift-selected parent sample, shown in gray, was drawn from the DR14 quasar catalog (Pâris et al. 2018). The three objects at low redshift are previously identified, well-known FeLoBALQs.

measured statistically significant blueshifts in the Fe II emission in J1214+2803 and J1448+4043 (by 330 and 740 km s^{-1}, respectively). While the cosmological redshift of J1448+4043 remains uncertain because there are no low-ionization Narrow Line Region (NLR) reference lines, [O II] was observed in the J1214+2803 spectrum, and the redshift could be measured securely. To measure the emission line properties of these four objects, we assumed that they are physically similar and then used the values of the parameters that could be measured in some objects to model other objects. Specifically, [O III] could be fully constrained by a single pair of Gaussians in position, intensity, and width in both J1030+3120 and J1044+3656. The [O III] was too obscured to be fully constrained in J1214+2803 and J1448+4043. The median value of the [O III] FWHM for J1030+3120 and J1044+3656 was approximately 2000 km s^{-1}. So, for J1214+2803 and J1448+4043, the FWHM was fixed at that value, and the intensity and position were modeled. The plots of the spectra and their model fits are given in Figure 3. The measured values of the emission line parameters are given in Table 1.

In some objects, the Fe II and/or [O III] emission was weak. We used the F-test (Bevington 1969) to gauge the statistical significance of these parameters in each model for both the FeLoBALQ and comparison samples. We used a significance cutoff of $p = 0.05$. We found that 40 and 15 (30% and 50%) of the comparison and FeLoBALQ samples did not statistically require the Fe II emission. We found that 12 and eight (16% and 27%) of the comparison and FeLoBALQ samples did not statistically require the [O III] emission.

No stellar population was apparent in the spectra of most of the FeLoBAL and comparison sample objects, so we did not include a young stellar population in our model. We reasoned that because the S/N of many of our spectra is low, an additional continuum component could not be robustly constrained. Not including this component, assuming that it is present in some objects, adds scatter to the equivalent and velocity widths of both the FeLoBALQ and comparison samples.

Several emission line properties were derived from the optical model fitting results; these are compiled in Table 1 for the FeLoBALQs. The total [O III] luminosity was computed from the [O III] λ5007 line flux alone. We computed the parameter $R_{\rm Fe\,II}$, commonly defined as the ratio of the Fe II equivalent width between 4434 and 4684 Å to the broad Hβ equivalent width. We followed the methodology of Zakamska & Greene (2014) to extract the [O III] median velocity offset v_{50} and velocity width w_{80}. Briefly, from the normalized cumulative function of the broad Hβ model profile, the velocities at 0.1, 0.5, and 0.9 were identified. The velocity at 0.5 is assigned to v_{50}, and w_{80} is the difference between the velocities at 0.1 and 0.9. It is important to note that, unlike Zakamska & Greene (2014) and similar studies of obscured quasars, the quality of these measurements varied dramatically throughout our sample and are not very robustly measured in objects with very strong Fe II and weak [O III].

We estimated the bolometric luminosity using the estimate of the rest-frame flux density at 3 μm and the bolometric correction derived by Gallagher et al. (2007). This bolometric correction was derived from 259 quasars with $0.14 < z < 5.22$ and estimated log bolometric luminosities $45.1 < \log L_{\rm Bol} < 47.4$ [erg s^{-1}] with a median value of 46.4. Our estimated bolometric luminosities fall in the range $45.1 < \log L_{\rm Bol} < 46.2$ with a median value of 46.2. Although our objects are somewhat less luminous than the quasars considered by Gallagher et al. (2007), the difference in median is only 0.2 dex. We obtained the 3 μm flux density from the Wide-field Infrared Survey Explorer photometry by doing a log-linear interpolation. For objects in this redshift range (0.7–0.97), 3 μm falls near the W2 effective wavelength (4.6 μm), and the W2 magnitude was generally measured with a good S/N in this sample of relatively nearby objects.

The black hole mass estimate requires an estimate of the radius of the Hβ-emitting broad-line region. We used the formalism given by Bentz et al. (2006). The flux density at 5100 Å was calculated from the power-law model component of the emission line model fits and then used to estimate the radius of the Hβ-emitting region. We did not correct for reddening intrinsic to the quasar; therefore, objects with significantly reddened spectra will have somewhat underestimated black hole masses. The black hole mass was estimated using the FWHM of the Hβ line and following the formalism of Collin et al. (2006). In particular, we used their Equation (7) to estimate the scale factor f based on the FWHM of the Hβ line.

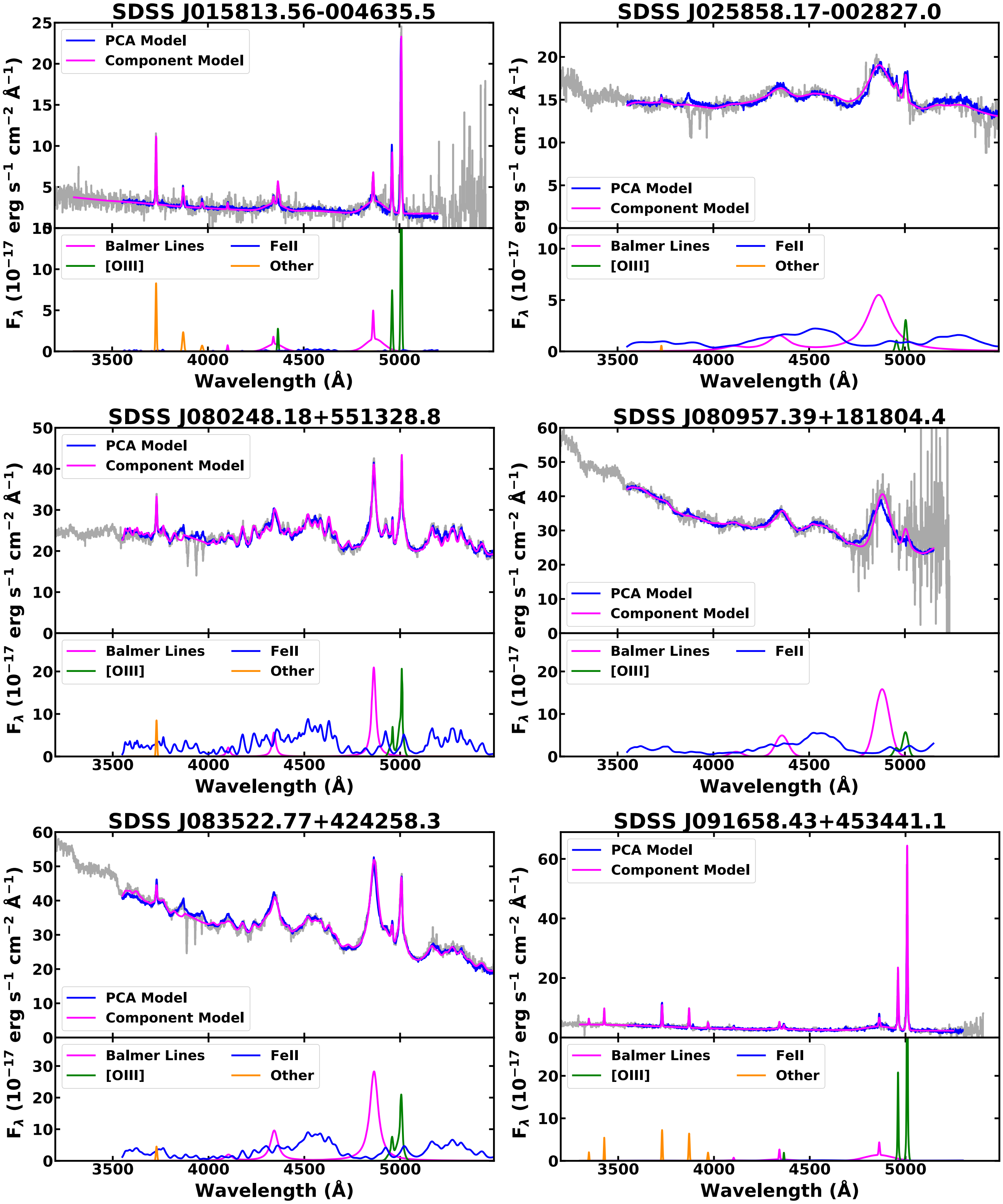

Figure 3. Optical portion of the FeLoBALQ sample spectra overlaid with the best-fitting model spectrum. Both the component-based emission line (Section 2.2) and the principal component eigenvector (Section 2.3) model fits are shown. The lower panels show the components from the component-based model. All five of the component figures are available in the figure set.

(The complete figure set (5 images) is available.)

We used the estimated black hole mass and bolometric luminosity to compute the size of the 2800 Å continuum emission region following the procedure described in Section 6.1 of Leighly et al. (2019). To summarize, we used a simple sum-of-blackbodies accretion disk model (Frank et al. 2002) and assigned the 2800 Å radius to be the location where the radially

Table 1
Spectral Fitting Results

SDSS Object Name	Hβ FWHM (km s^{-1})	Hβ EW (Å)	$R_{\text{Fe II}}$	[O III] EW (Å)	[O III] V_{50} (km s^{-1})	[O III] W_{80} (km s^{-1})	[O III] Luminosity (erg s^{-1})	log L_{Bol} (erg s^{-1})	BH Mass ($M_{\odot}$)	Edd. Ratio	$E1$ Parameter[a]
015813.56–004635.5	6850^{+1180}_{-700}	$93^{+18.}_{-9.8}$	$0.196^{+0.115}_{-0.076}$	$106.5^{+4.2}_{-3.8}$	67^{+9}_{-8}	530^{+20}_{-20}	$42.87^{+0.02}_{-0.02}$	45.11 ± 0.11	$8.57^{+0.13}_{-0.11}$	$-1.56^{+0.13}_{-0.11}$	$-2.45^{+0.39}_{-0.42}$
025858.17–002827.0	9000^{+290}_{-290}	$96^{+3.1}_{-3.2}$	$0.378^{+0.045}_{-0.039}$	$4.3^{+0.5}_{-0.5}$	-261^{+58}_{-52}	1110^{+160}_{-140}	$42.32^{+0.05}_{-0.06}$	46.36 ± 0.01	$8.64^{+0.04}_{-0.05}$	$-0.38^{+0.04}_{-0.05}$	$1.10^{+0.16}_{-0.14}$
080248.18+551328.8	1560^{+30}_{-30}	$42^{+0.5}_{-0.6}$	$1.67^{+0.045}_{-0.045}$	$17.8^{+0.6}_{-0.6}$	-111^{+21}_{-23}	1670^{+60}_{-60}	$42.82^{+0.01}_{-0.01}$	46.56 ± 0.009	$7.57^{+0.04}_{-0.04}$	$0.9^{+0.04}_{-0.04}$	$1.01^{+0.039}_{-0.037}$
080957.39+181804.4	5400^{+140}_{-150}	$56^{+1.7}_{-1.8}$	$0.743^{+0.069}_{-0.062}$	$9^{+0.9}_{-1.0}$	-320^{+140}_{-182}	2180^{+0}_{0}	$42.99^{+0.04}_{-0.05}$	46.41 ± 0.02	$7.97^{+0.04}_{-0.04}$	$0.35^{+0.04}_{-0.04}$	$0.98^{+0.13}_{-0.12}$
083522.77+424258.3	3250^{+40}_{-40}	$91^{+0.8}_{-0.9}$	$0.696^{+0.017}_{-0.018}$	$22.9^{+0.7}_{-0.7}$	-274^{+21}_{-21}	2100^{+80}_{-90}	$43.18^{+0.01}_{-0.01}$	46.58 ± 0.01	$8.33^{+0.04}_{-0.04}$	$0.15^{+0.04}_{-0.04}$	0.05 ± 0.04
091658.43+453441.1	$10, 390^{+1200}_{-700}$	$102^{+12.}_{-7.8}$	$0.121^{+0.068}_{-0.107}$	$175.9^{+20.8}_{-21.4}$	36^{+4}_{-6}	460^{+60}_{-40}	$43.22^{+0.05}_{-0.05}$	45.53 ± 0.03	$8.9^{+0.10}_{-0.07}$	$-1.47^{+0.1}_{-0.07}$	$-3.33^{+0.44}_{-0.67}$
094404.25+500050.3	3800^{+620}_{-520}	$35^{+4.7}_{-4.0}$	$1.308^{+0.262}_{-0.232}$	$4.9^{+1.3}_{-1.2}$	-245^{+221}_{-225}	1840^{+470}_{-440}	$42.1^{+0.1}_{-0.12}$	46.17 ± 0.02	$8.46^{+0.13}_{-0.15}$	$-0.39^{+0.13}_{-0.15}$	$2.02^{+0.32}_{-0.27}$
102226.70+354234.8	7360^{+740}_{-670}	$59^{+5.4}_{-5.0}$	$0.538^{+0.11}_{-0.10}$	$6.8^{+0.9}_{-0.9}$	-537^{+75}_{-82}	1630^{+290}_{-260}	$42.08^{+0.06}_{-0.06}$	46.05 ± 0.02	$8.66^{+0.09}_{-0.10}$	$-0.7^{+0.09}_{-0.10}$	0.97 ± 0.21
103036.92+312028.8	7090^{+110}_{-90}	$53^{+2.0}_{-0.7}$	$0.868^{+0.056}_{-0.04}$	$4^{+0.4}_{-0.4}$	-1581^{+76}_{-71}	2130^{+140}_{-140}	$42.51^{+0.04}_{-0.05}$	46.64 ± 0.01	8.57 ± -0.04	-0.02 ± 0.04	$1.86^{+0.12}_{-0.09}$
103903.03+395445.8	3930^{+140}_{-170}	58 ± 2.0	$0.075^{+0.091}_{-0.078}$	$63^{+4.9}_{-5.2}$	-252^{+25}_{-26}	1250^{+130}_{-120}	$42.91^{+0.03}_{-0.04}$	46.18 ± 0.02	$8.44^{+0.05}_{-0.06}$	$-0.35^{+0.05}_{-0.06}$	$-2.76^{+0.72}_{-0.65}$
104459.60+365605.1	3460^{+30}_{-40}	$57^{+0.4}_{-0.5}$	$0.832^{+0.018}_{-0.017}$	$4.0^{+0.3}_{-0.2}$	-1405^{+83}_{-108}	2620^{+250}_{-190}	42.57 ± 0.03	46.71 ± 0.009	7.82 ± 0.03	0.8 ± 0.03	1.83 ± 0.06
112526.12+002901.3	6800^{+140}_{-130}	$46^{+0.9}_{-0.8}$	$0.452^{+0.013}_{-0.019}$	$36.8^{+0.9}_{-1.0}$	-344^{+27}_{-22}	2920^{+210}_{-170}	43.27 ± 0.01	46.28 ± 0.02	8.67 ± 0.05	-0.48 ± 0.05	$-0.76^{+0.03}_{-0.04}$
112828.31+011337.9	$11, 550^{+1160}_{-360}$	$70^{+8.7}_{-2.1}$	$0.125^{+0.064}_{-0.056}$	$27.9^{+4.5}_{-4.3}$	-42^{+38}_{-20}	830^{+380}_{-90}	43.15 ± 0.07	46.17 ± 0.02	$8.29^{+0.08}_{-0.05}$	$-0.22^{+0.08}_{-0.05}$	$-1.57^{+0.39}_{-0.46}$
120049.54+632211.8	$10, 060^{+730}_{-680}$	$47^{+4.6}_{-4.2}$	$0.091^{+0.062}_{-0.051}$	$99.3^{+7.4}_{-7.6}$	2^{+8}_{-10}	790^{+50}_{-40}	43.5 ± 0.03	45.89 ± 0.02	8.3 ± 0.07	-0.53 ± 0.07	$-3.03^{+0.45}_{-0.56}$
120815.03+624046.4	8140^{+420}_{-330}	$78^{+3.4}_{-2.9}$	$0.093^{+0.045}_{-0.046}$	$144.9^{+10.7}_{-10.6}$	-11^{+6}_{-3}	590 ± 40	43.13 ± 0.03	45.42 ± 0.04	8.31 ± 0.05	-0.99 ± 0.05	$-3.37^{+0.34}_{-0.49}$
121231.47+251429.1	2100 ± 120	42.0 ± 1.8	$1.102^{+0.111}_{-0.103}$	$5.6^{+0.6}_{-0.5}$	-240 ± 34	900^{+140}_{-120}	42.16 ± 0.04	46.34 ± 0.01	$7.99^{+0.06}_{-0.07}$	$0.25^{+0.06}_{-0.07}$	1.76 ± 0.12
121442.30+280329.1	7480 ± 90	56 ± 0.7	$1.112^{+0.045}_{-0.042}$	3.8 ± 0.3	-657^{+103}_{-123}	2180	$42.47^{+0.03}_{-0.04}$	46.47 ± 0.01	8.27 ± 0.03	0.1 ± 0.03	$2.14^{+0.09}_{-0.08}$
124014.04+444353.4	$10, 050^{+1330}_{-1020}$	$87^{+11.0}_{-9.9}$	$0.083^{+0.065}_{-0.084}$	$162.4^{+23.0}_{-23.6}$	86^{+17}_{-12}	790^{+100}_{-70}	$43.25^{+0.06}_{-0.07}$	45.66 ± 0.03	$8.49^{+0.11}_{-0.10}$	$-0.92^{+0.11}_{-0.10}$	$-3.56^{+0.55}_{-0.65}$
132117.24+561724.5	6600^{+200}_{-150}	$74^{+2.0}_{-2.1}$	$0.156^{+0.015}_{-0.06}$	$75.1^{+2.4}_{-2.1}$	5^{+4}_{-5}	720 ± 20	43.09 ± 0.01	45.39 ± 0.04	$8.49^{+0.05}_{-0.04}$	$-1.2^{+0.05}_{-0.04}$	$-2.31^{+0.08}_{-0.40}$
132401.53+032020.5	7360^{+330}_{-310}	$60^{+2.2}_{-2.1}$	$0.168^{+0.055}_{-0.046}$	$81^{+8.0}_{-8.1}$	165^{+12}_{-15}	1200^{+80}_{-60}	$43.61^{+0.04}_{-0.05}$	46.30 ± 0.02	8.3 ± 0.05	-0.1 ± 0.05	$-2.33^{+0.26}_{-0.27}$
133632.45+083059.9	4240^{+170}_{-330}	$48^{+1.4}_{-3.2}$	$0.999^{+0.090}_{-0.091}$	2.6 ± 0.5	9^{+1715}_{-90}	2180	$42.05^{+0.08}_{-0.10}$	46.1 ± 0.01	$8.21^{+0.05}_{-0.08}$	$-0.2^{+0.05}_{-0.08}$	$2.39^{+0.22}_{-0.20}$
135525.24+575312.7	7560^{+680}_{-650}	$97^{+7.3}_{-6.2}$	$0.24^{+0.039}_{-0.239}$	$104.1^{+8}_{-12.4}$	-45^{+20}_{-82}	1320^{+1380}_{-120}	$42.78^{+0.03}_{-0.05}$	45.63 ± 0.03	$8.47^{+0.08}_{-0.09}$	$-0.93^{+0.08}_{-0.09}$	$-2.26^{+0.18}_{-0.67}$
135640.34+452727.2	9540^{+990}_{-900}	140^{+24}_{-20}	$0.57^{+0.16}_{-0.13}$	27.5 ± 3.4	-110^{+12}_{-11}	640^{+56}_{-50}	$42.67^{+0.05}_{-0.06}$	46.03 ± 0.01	$8.90^{+0.09}_{-0.10}$	$-0.96^{+0.10}_{-0.09}$	$-0.29^{+0.25}_{-0.23}$
144800.15+404311.7	7670 ± 100	$44^{+0.6}_{-0.5}$	1.196 ± 0.033	1.6 ± 0.2	-2084^{+120}_{-99}	2180	42.49 ± 0.05	46.81 ± 0.009	8.55 ± 0.04	0.16 ± 0.04	3.00 ± 0.11
151708.94+232857.5	$10, 080^{+1170}_{-640}$	$110^{+10}_{-6.0}$	$0.53^{+0.05}_{-0.1}$	$70.5^{+3.1}_{-3.0}$	48^{+14}_{-12}	1320^{+60}_{-90}	42.72 ± 0.02	45.92 ± 0.02	$9.02^{+0.1}_{-0.07}$	$-1.2^{+0.1}_{-0.07}$	$-1.24^{+0.08}_{-0.18}$
152737.17+591210.1	$16, 790^{+1170}_{-1080}$	$78^{+8.7}_{-7.8}$	$0.32^{+0.049}_{-0.062}$	5.4 ± 1	-30^{+78}_{-77}	1330^{+220}_{-210}	42.52 ± 0.08	46.60 ± 0.01	9.28 ± 0.07	-0.78 ± 0.07	$0.76^{+0.21}_{-0.24}$
153145.01+485257.2	4460^{+340}_{-350}	39 ± 3.2	$0.239^{+0.057}_{-0.201}$	$52.3^{+3.9}_{-4.4}$	-10^{+11}_{-15}	640^{+120}_{-60}	$42.82^{+0.03}_{-0.04}$	45.86 ± 0.02	$8.67^{+0.08}_{-0.09}$	$-0.9^{+0.08}_{-0.09}$	$-1.62^{+0.21}_{-0.65}$
164419.75+530750.4	$10, 590^{+290}_{-160}$	$54^{+1.3}_{-0.9}$	$0.176^{+0.043}_{-0.020}$	$12.2^{+0.5}_{-0.7}$	-79^{+17}_{-27}	1730^{+290}_{-420}	$42.95^{+0.02}_{-0.03}$	46.38 ± 0.009	$8.97^{+0.05}_{-0.04}$	$-0.69^{+0.05}_{-0.04}$	$-0.51^{+0.19}_{-0.11}$
213537.44–032054.8	8270^{+380}_{-370}	$185^{+5.2}_{-5.0}$	0.038 ± 0.01	$33.2^{+1.7}_{-1.8}$	5^{+13}_{-12}	870^{+110}_{-70}	$43.06^{+0.02}_{-0.03}$	46.41 ± 0.01	8.75 ± 0.06	-0.44 ± 0.06	$-2.74^{+0.20}_{-0.27}$
230730.69+111908.5	8430^{+340}_{-280}	$102^{+4.4}_{-3.2}$	$0.564^{+0.120}_{-0.104}$	$46.7^{+3.3}_{-3.7}$	-174^{+34}_{-31}	1480^{+140}_{-170}	$42.92^{+0.03}_{-0.04}$	46.31 ± 0.02	8.69 ± 0.05	-0.47 ± 0.05	-0.80 ± 0.18

Note.
[a] The $E1$ parameter is defined in Section 3.1.

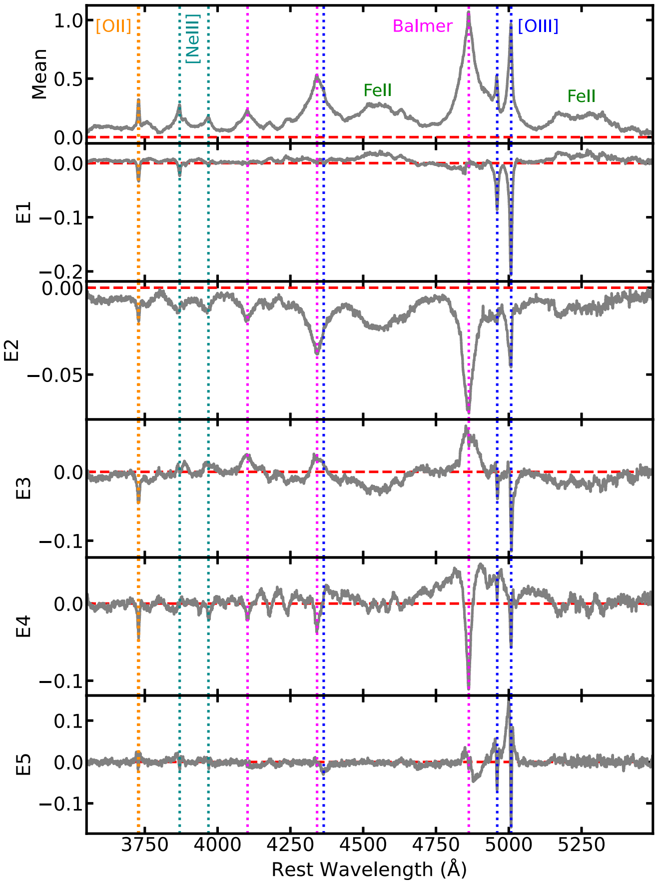

Figure 4. Mean spectrum and first five eigenvectors constructed from the 132 objects in the comparison sample. Principal emission lines are labeled.

weighted brightness dropped by a factor of *e* from the peak value. This estimate may not be accurate for the full range of Eddington ratios represented by the sample, since the structure of the accretion disk is thought to be different for very low and very high accretion rates (e.g., Giustini & Proga 2019).

The uncertainties in the derived parameters were estimated using the `Sherpa` model fit errors. Because the errors produced by `Sherpa` were sometimes asymmetric, we used a Monte Carlo scheme to propagate the errors. Specifically, we created 10,000 instances of each parameter varying the value within the errors, then computed the derived property and extracted the 1σ errors from the cumulative distributions.

We investigated whether there are any systematic differences in the properties measured in this paper between the previously and newly classified BALQs using the two-sample Kolmogorov–Smirnov (K-S) test and the two-sample Anderson–Darling (A-D) test. Among those 17 properties, we found significant ($p < 0.05$) differences in only three properties. The Spectral Principal Components Analysis (SPCA) eigenvector 4 coefficient (Section 2.3) was lower in the new objects. Examining the plot of the SPCA eigenvectors (Figure 4) shows that this means that objects with narrow Fe II emission lines are preferentially represented among the previously identified objects. The median bolometric luminosity was 0.44 dex lower among the new FeLoBALQs compared with the previously known objects. This reflects the fact that the brightest objects in a sample are usually identified first, likely because they have higher-S/N spectra. Finally, the size of the 2800 Å emission region of the new objects is 0.1 dex lower than the previously known objects, likely a consequence of the lower luminosities.

The 132 comparison sample spectra were subjected to the same analysis.

2.3. Principal Component Analysis

While spectral decomposition using emission line profiles and templates is a widely used and valid approach, model dependence must be present. Decomposition using spectral principal components provides a complementary and less model-dependent analysis.

We created the principal components using the 132 comparison spectra described in Section 2.1. We preprocessed the spectra by dividing by the fitted continuum flux density at 4950 Å and subtracting the scaled continuum obtained from spectral fitting. This procedure of subtracting the continuum differs from many applications of PCA (e.g., Shang et al. 2003; Pâris et al. 2011) and has the advantage that the considerable variance present due to variations in continuum slope does not contaminate the emission line eigenvectors.

We used `EMPCA` (Bailey 2012) to compute the eigenvectors. This method has several advantages over the traditional singular value decomposition method. Principally, the method weights the data using the uncertainties, and missing data are given a weight of zero. This is important because PCA methods find the regions of the data that have the most variance, and noise can infiltrate the eigenvectors that describe the most variance in the data set (e.g., Figure 5 in Bailey 2012). The first and second eigenvectors modeled 29% and 9.9% of the variance, respectively. We retain the first five eigenvectors to model the variance of the emission lines; subsequent ones each model less than 1% of the variance. The mean and first five eigenvectors are shown in Figure 4.

The mean spectrum and eigenvectors offer no great surprises. The first eigenvector shows a strong anticorrelation between [O III] and Fe II and is essentially the Boroson & Green (1992) first eigenvector. This construct is historically known as Eigenvector 1, and repeatedly found in PCA analysis of optical rest-frame quasar spectra (e.g., Sulentic et al. 2000; Grupe 2004; Ludwig et al. 2009; Wolf et al. 2020). The second eigenvector shows strong Balmer lines and Fe II emission. The fourth eigenvector is interesting because it includes very narrow Fe II lines and therefore should be strongly negative when modeling the narrow-line Seyfert 1 galaxies in our sample. It is notable that the [O II] line and other very narrow lines are clearly present in the eigen spectra; this is a consequence of the careful redshift correction.

We used the mean spectrum and first five eigenvectors to fit the 30 FeLoBAL spectra and 132 comparison sample spectra. The spectra were prepared for spectral fitting by being normalized by the same value used to process the spectra for PCA analysis. The model is comprised of a linear combination of the same continuum model used for each spectrum in Section 2.2, the mean emission line spectrum, and the five eigenvectors, where the normalization of the mean emission line spectrum is frozen at a value of 1. The continuum normalization was left free to vary, as were the coefficients of the eigenvectors, which serve to modify the shape of the mean emission line spectrum.

3. Distribution Comparisons and Correlations

In this section, we compare the emission line properties of the FeLoBALQs with those of the comparison sample of unabsorbed quasars using cumulative distribution plots. We then examine the relationships among the optical and global parameters using Spearman rank correlations.

3.1. Distributions

We report the results of the two-sample K-S and A-D tests in Table 2. The K-S test reliably tests the difference between two distributions when the difference is large at the median values, while the A-D test is more reliable if the differences lie toward the maximum or minimum values (i.e., the median can be the same and the distributions different at larger and smaller values).[10] We also examined the relationships among the optical properties of our sample of FeLoBALQs and the comparison sample. The four pairs of columns in the table correspond to several different cases. The first pair gives the results for all of the data; the remainder are divided by the $E1$ parameter, which is described next.

The principal component analysis revealed that the dominant variance in the emission line properties arises from the anticorrelation between the [O III] and Fe II (Section 2.3). As noted above, this anticorrelation is common among samples of optical spectra of quasars and also appears among the UV emission lines and in other properties of quasars (e.g., Boroson & Green 1992; Francis et al. 1992; Brotherton et al. 1994; Corbin & Boroson 1996; Wills et al. 1999; Shang et al. 2003; Grupe 2004; Yip et al. 2004; Wang et al. 2006; Ludwig et al. 2009; Shen 2016). In this sample, we parameterize these properties using the [O III] equivalent width and the ratio of Fe II to Hβ (hereafter referred to as $R_{\mathrm{Fe\,II}}$; e.g., Shen & Ho 2014). The anticorrelation for the FeLoBALQs and comparison sample is seen in the left panel of Figure 5.

We created a summary statistic parameter that describes the anticorrelation. We computed the base-10 logarithm of $R_{\mathrm{Fe\,II}}$ and [O III]. For convenience, we computed the mean and standard deviation of both quantities from the comparison sample and used those values to scale and normalize both samples. We then used the bivariate correlated errors and intrinsic scatter method[11] (Akritas & Bershady 1996) to obtain the bisector of the two parameters. This method takes into account the uncertainty on both parameters. The bisector is more appropriate than a regression, since neither parameter can be identified as the dependent or independent variable. After scaling and normalization, the slope of the bisector is close to -1, as expected.

An alternative method for obtaining our summary statistic parameter takes into account the fact that [O III] and Fe II emission was not found to be statistically necessary in some objects using the F-test (Section 2.2). We evaluated the bisector using the methodology of Isobe et al. (1990), taking into account the statistically unnecessary values as upper limits using the likelihood given by Sawicki (2012). The relationship is shown in Figure 5. As expected, the bisector line is shifted slightly toward lower values of the $R_{\mathrm{Fe\,II}}$ and [O III] equivalent width. Noting that the summary statistic is defined for convenience and does not represent a physical relationship, we proceeded with the original bisector because it appears more representative of the data.

We then rotated the coordinate system so that the long axis of the bisector is horizontal. The result is shown in the right panel of Figure 5. We take the rotated X-axis value as our desired summary statistic, hereafter referred to as the "$E1$ parameter." Note that this parameter is closely related to the SPCA1 fit coefficients. As we will discuss in Section 3.3, the FeLoBALQs consist of two distinct populations simply divided at $E1 = 0$. In Table 2, we compare the FeLoBALQs with $E1 < 0$ and $E1 > 0$ with their unabsorbed sample counterparts, as well as with one another.

3.2. FeLoBALQs versus Unabsorbed Objects

3.2.1. Optical Properties

The Hβ emission line was parameterized using the FWHM and equivalent width. The cumulative distributions of the Hβ FWHM are plotted in Figure 6. The cumulative distributions for the FeLoBALQs and comparison sample are profoundly different (see Table 2), with the FeLoBALQs showing consistently larger FWHMs. There is a tendency for the FeLoBALQs to have smaller Hβ equivalent widths, but it is not statistically significant.

There is a statistically significant difference in the $R_{\mathrm{Fe\,II}}$ between the comparison sample and the FeLoBALQs for the $E1 < 0$ subsample. There are excess low-$R_{\mathrm{Fe\,II}}$ objects among the FeLoBALQs, as well as a hint of excess high-$R_{\mathrm{Fe\,II}}$ objects. We will return to this point in Section 3.3.

We used the [O III] equivalent width to quantify the strength of the [O III] emission line and v_{50} and w_{80} (defined in Section 2.2) to parameterize the profile shape. The distributions of the [O III] equivalent width are statistically significantly different; note that this is an excellent example of a pair of distributions that are found to be less significantly different using the K-S test ($p = 0.034$) compared with the A-D test ($p < 0.001$; the software that we used does not compute probabilities less than this value) due to the fact that the median of the distributions is not very different but the ends are. Specifically, there are many more FeLoBALQs with much larger and much smaller [O III] equivalent widths than the comparison sample. There are no statistical differences between the FeLoBALQs and the comparison sample for v_{50} and w_{80}.

3.2.2. The SPCA Eigenvector Coefficients

We compared the fit coefficients for the model using the first four SPCA eigenvectors (Section 2.3) in Figure 7, and the K-S and A-D statistics are given in Table 2. We found that the distributions for the FeLoBALQs differ from those of the comparison sample for the first three coefficients.

3.2.3. Global Properties

We investigated the distributions of several global properties of the quasars, including the integrated [O III] luminosity, bolometric luminosity, black hole mass (computed as described in Section 2.2), Eddington ratio $L_{\mathrm{Bol}}/L_{\mathrm{Edd}}$, and size of the 2800 Å continuum emission region. The distributions are shown in Figure 8, and the K-S and A-D statistics are given in Table 2. Most of these properties are statistically consistent between the FeLoBALQs and the comparison sample objects. The exception is the A-D test for the Eddington ratio; the FeLoBALQs have an excess of objects at high and low $L_{\mathrm{Bol}}/L_{\mathrm{Edd}}$ values.

---

[10] For example, https://asaip.psu.edu/articles/beware-the-kolmogorov-smirnov-test/.

[11] Using https://github.com/rsnemmen/BCES; Nemmen et al. (2012).

Table 2
Parameter Distribution Comparison

Parameter Name	FeLoBALQs versus Comparison						FeLoBALQs	
	All (30/132)		$E1 < 0$ (17/61)		$E1 > 0$ (13/71)		$E1 < 0$ vs. $E1 > 0$[a]	
	K-S[b]	A-D[c]	K-S[b]	A-D[c]	K-S[b]	A-D[c]	K-S[b]	A-D[c]
Hβ FWHM	**0.56/1.5 × 10^{-7}**	**18.0/<0.001**	**0.65/6.3 × 10^{-6}**	**13.3/<0.001**	**0.42/0.029**	**4.25/6.5 × 10-3**	0.43/0.09	**3.3/0.014**
Hβ EW	0.25/0.088	0.99/0.13	0.24/0.37	0.19/>0.25	0.37/0.068	1.1/0.12	**0.48/0.050**	**2.65/0.027**
$R_{\text{Fe II}}$	**0.35/3.6 × 10^{-3}**	**4.5/5.4 × 10^{-3}**	**0.60/4.9 × 10^{-5}**	**7.3/<0.001**	0.14/0.97	−0.83/>0.25	**0.77/6.8 × 10^{-5}**	**11.8/<0.001**
[O III] EW	**0.28/0.034**	**6.5/1.0 × 10^{-3}**	**0.47/3.0 × 10^{-3}**	**8.0/<0.001**	**0.61/2.1 × 10^{-4}**	**8.3/<0.001**	**0.94/2.3 × 10^{-7}**	**14.1/<0.001**
[O III] V_{50} (km s^{-1})	0.25/0.084	1.8/0.056	**0.44/6.8 × 10^{-3}**	**5.3/2.7 × 10^{-3}**	0.29/0.26	1.25/0.10	**0.67/1.2 × 10^{-3}**	**7.3/<0.001**
[O III] W_{80} (km s^{-2})	0.15/0.61	−0.50/>0.25	**0.40/0.021**	**2.4/0.032**	**0.40/0.040**	**2.0/0.050**	**0.67/1.2 × 10^{-3}**	**7.5/<0.001**
SPCA $E1$	**0.33/7.2 × 10^{-3}**	**5.0/3.5 × 10^{-3}**	**0.53/6.0 × 10^{-4}**	**9.8/<0.001**	0.38/0.062	**2.0/0.048**	**1.0/1.7 × 10^{-8}**	**14.8/<0.001**
SPCA $E2$	**0.40/4.7 × 10^{-4}**	**5.1/3.1 × 10^{-3}**	0.21/0.53	−0.64/>0.25	**0.66/4.8 × 10^{-5}**	**8.4/<0.001**	**0.48/0.050**	**2.7 /0.026**
SPCA $E3$	**0.37/1.5 × 10^{-3}**	**10.3/<0.001**	**0.63/1.3 × 10^{-5}**	**10.9/<0.001**	**0.39/0.048**	1.3/0.09	**0.69/8.0 × 10^{-4}**	**5.5/2.3 × 10^{-3}**
SPCA $E4$	0.14/0.70	−0.14/>0.25	**0.38 /0.032**	**3.0/0.020**	0.35/0.10	1.2/0.10	**0.55/0.014**	**3.6/0.011**
$E1$ parameter	**0.34/4.7 × 10^{-3}**	**5.7/1.9 × 10^{-3}**	**0.57/1.6 × 10^{-4}**	**9.0/<0.001**	**0.49/6.9 × 10^{-3}**	**5.0/3.4 × 10^{-3}**	**1.0/1.7 × 10^{-8}**	**14.8/<0.001**
Hβ FWHM deviation	**0.33/7.9 × 10^{-3}**	**6.8/<0.001**	**0.36/0.050**	**3.0/0.019**	**0.42/0.026**	**3.5/0.012**	0.34/0.29	0.26/>0.25
[O III] luminosity	0.17/0.41	−0.07/>0.25	0.25/0.33	0.48/0.21	0.25 /0.43	−0.58/>0.25	**0.77/6.8 × 10^{-5}**	**9.0/<0.001**
M_{BH}	0.12/0.79	−0.67/>0.25	0.31/0.12	0.91/0.14	0.27/0.32	0.88/0.14	**0.59/6.0 × 10^{-3}**	**5.5/2.2 × 10^{-3}**
L_{Bol}	0.11/0.91	−0.72/>0.25	0.31/0.12	1.65/0.068	**0.47/9.0 × 10^{-3}**	**3.6/0.011**	**0.65/1.7 × 10^{-3}**	**8.5/<0.001**
$L_{\text{Bol}}/L_{\text{Edd}}$	0.20/0.23	**3.1/0.018**	0.35/0.06	**3.5/0.013**	**0.50/4.2 × 10^{-3}**	**6.9/<0.001**	**0.72/2.9 × 10^{-4}**	**9.7/<0.001**
R_{2800} [pc]	0.16/0.48	0.16/>0.25	0.30/0.16	0.43/0.22	0.17/0.86	−0.76/>0.25	0.18/0.93	−0.77/>0.25

Notes.

[a] The optical data from the $E < 0$ ($E > 0$) FeLoBALQ subsamples include 17 (13) objects.

[b] The K-S two-sample test. Each entry has two numbers: the first is the value of the statistic, and the second is the probability that the two samples arise from the same parent sample. Bold indicates entries that yield $p < 0.05$.

[c] The A-D two-sample test. Each entry has two numbers: the first is the value of the statistic, and the second is the probability that the two samples arise from the same parent sample. Note that the implementation used does not compute a probably larger than 0.25 or smaller than 0.001. Bold indicates entries that yield $p < 0.05$.

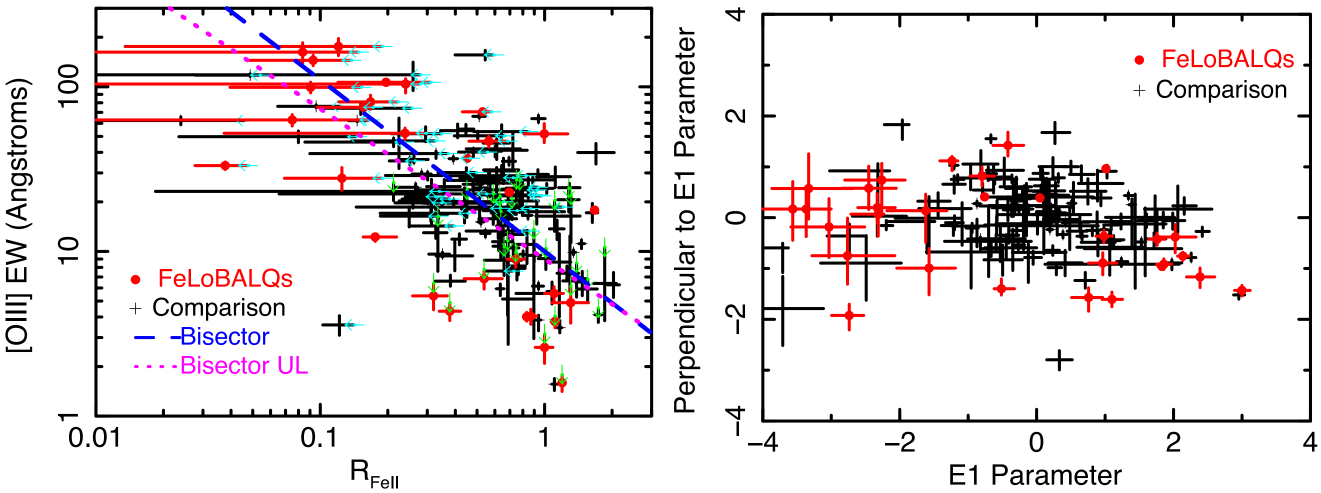

Figure 5. Construction of the $E1$ parameter. Left: anticorrelation of the ratio of the Fe II and Hβ fluxes with the [O III] equivalent width. Arrows mark the measurements deemed statistically insignificant using the F-test (Section 2.2). The new coordinate system was defined by the bisector slope computed from the normalized and scaled log values of these parameters. The relationship is given by $E1 = 0.679(\log_{10}(R_{\rm Fe\,II}) + 0.270) - 0.735(\log_{10}([{\rm O\,III}]{\rm EW}) - 1.288)$. Right: data after rotation to the new coordinate system. The bisector line now lies along the x-axis and thereby defines the $E1$ parameter.

3.3. Evidence for Two Populations of FeLoBALQs

Examination of the right panel of Figure 5 reveals that the FeLoBALQs are not distributed evenly in the $E1$ parameter. While the comparison sample object distribution peaks at $E1 \sim 0$, declining toward lower and higher values, the FeLoBALQ $E1$ values straddle both sides of the center. The K-S (A-D) tests yield a probability of 0.46% (0.19%) that the two samples were drawn from the same parent distribution. The differences in the distribution are visualized in the histogram and cumulative distributions shown in the top panels of Figure 9.

The FeLoBALQ $E1$ parameter distribution appears to be bimodal, but statistical tests do not establish bimodality. We first used the Hartigan & Hartigan (1985) dip test. This test could not reject a unimodal distribution ($p = 0.22$). We also used the Muratov & Gnedin (2010) GMM method[12] (Muratov & Gnedin 2010). The method fits a two-component Gaussian mixture model (GMM) to the data and compares the result to a one-component GMM using a likelihood ratio. A bootstrap method was used to gauge the robustness of the result. The $E1$ parameter from the FeLoBALQs yielded a probability of $p = 0.045$ that the distribution is unimodal rather than bimodal. The best-fitting two-component GMM[13] is seen as the dashed green line in the top left panel of Figure 9. The Gaussian parameters were $\mu_1 = 1.54$, $\mu_2 = -2.0$, $\sigma_1 = 0.78$, $\sigma_2 = 1.09$, $N_1 = 0.42$, and $N_2 = 0.58$. Note the significant limitation of this method; it assumes that the two distributions are Gaussian, and there is no reason to believe that they should be. Indeed, the cumulative distribution functions shown in the top right panel of Figure 9 indicate that the two-Gaussian approximation is only an approximate representation of the $E1$ parameter from the FeLoBALQs.

We divided the samples in two, depending on the sign of the $E1$ parameter. Note that $E1 = 0$ is a representative dividing point because the log [O III] equivalent width and $R_{\rm Fe\,II}$ were normalized and scaled before $E1$ was computed. There are 17 (61) and 13 (71) FeLoBALQs (comparison sample objects) with an $E1$ parameter of less than and greater than zero, respectively. The weighted mean spectra for these two groups compared with the mean comparison sample spectrum are shown in the bottom panels of Figure 9. The differences are notable. The FeLoBALQ objects with $E1$ parameters less than zero are characterized by stronger [O III] and weaker Fe II than the comparison sample average spectrum, while the objects with $E1$ parameters greater than zero have similar Fe II emission, weaker Balmer lines, and weaker [O III]. It is also notable that the $E1 < 0$ mean spectrum shows Balmer absorption, seen in the notches in the mean spectrum near 4830 and 4330 Å, while the $E1 > 0$ mean spectrum shows Ca II and He I* absorption, observed in the scrum of absorption lines near 3900 Å. These different lines point to differences in the physical conditions of the absorbing outflow (Choi et al. 2022). We note that because these are weighted average spectra, they reflect the properties of the objects with the best S/N spectra.

In Section 3, we compare the distributions of the parameters of the FeLoBALQs with those of the comparison sample. Here we perform the same comparison but divide the two samples by the $E1$ parameter. We do this because if the FeLoBALQs are comprised of two classes, then they may differ in different ways from the similarly selected comparison sample; we do see this behavior in the parameter comparison below. We also compare the two groups of FeLoBALQs because significant differences indicate a defining or correlated characteristic property of the two groups.

The cumulative distribution of the $E1$ parameter is shown in Figure 10. Blue (red) lines identify the $E1 > 0$ ($E1 < 0$) objects, with solid (dashed) lines denoting the FeLoBALQs (comparison samples). As expected, dividing the data by $E1$ results in an enormous difference in the $E1$ parameter distribution.

There are significant differences between the FeLoBAL classes among all of the emission line properties (Figure 6). Some of these are expected; for example, the $R_{\rm Fe\,II}$ and [O III] equivalent widths were used to define the $E1$ parameter. While as a group, the [O III] kinematic properties (velocity offset v_{50} and w_{80}) are consistent between the FeLoBALQs and comparison objects, they are significantly different between the $E1 < 0$ and $E1 > 0$ FeLoBALQs. The $E1 > 0$ ($E1 < 0$)

---

[12] http://www-personal.umich.edu/~ognedin/gmm/

[13] https://scikit-learn.org/stable/modules/mixture.html

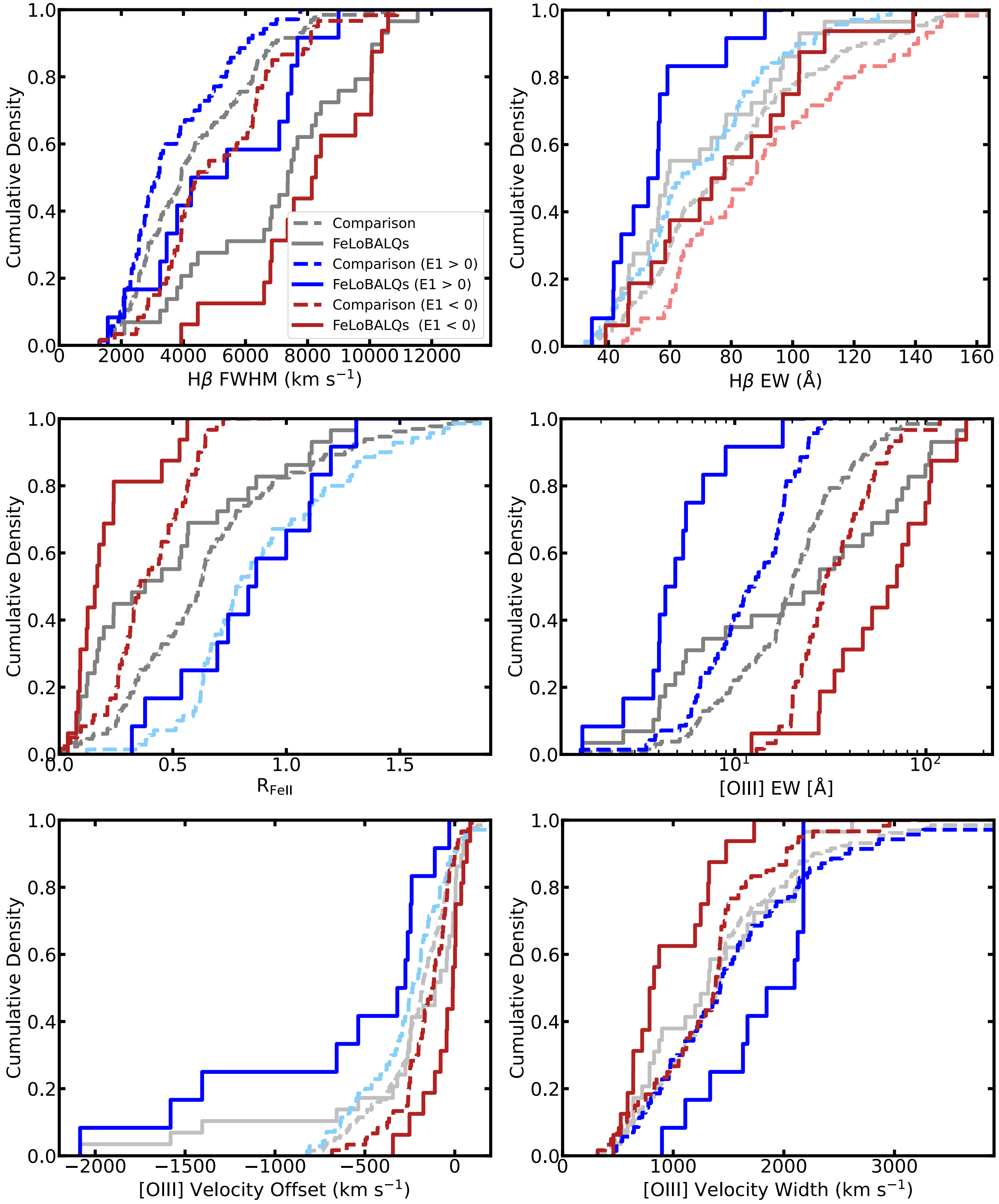

Figure 6. Cumulative distribution plots of the optical emission line parameters. The data are sampled in three ways: the gray lines show the full FeLoBALQ and comparison samples, and the blue (red) lines show the FeLoBALQ and comparison samples for $E1$ parameter $E1 > 0$ ($E1 < 0$). The $E1$ parameter is introduced in Section 3 and discussed in Section 3.3. The K-S and A-D statistics for four different comparisons are given in Table 2. Distributions that are significantly different ($p < 0.05$) are shown in dark red, dark blue, or dark gray, while distributions that are not significantly different are shown in pale colors. The full sample distributions are statistically significantly different for Hβ FWHM, $R_{\rm Fe\ II}$, and [O III] equivalent width. The FeLoBALQs partitioned by the $E1$ parameter are statically significantly different for all properties.

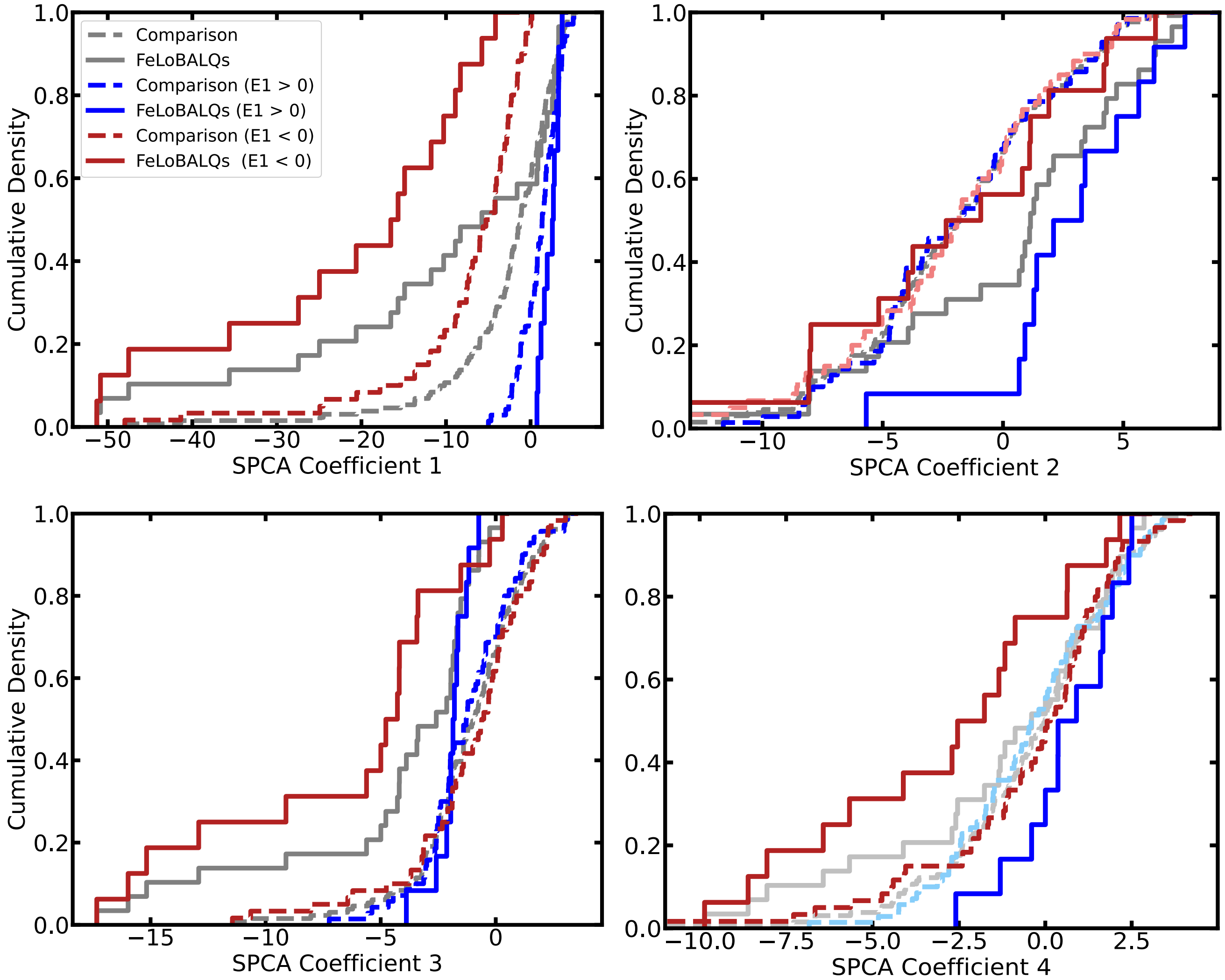

Figure 7. Cumulative distribution plots of the SPCA fit coefficients. The colors and line styles are the same as in Figure 6, and the K-S and A-D statistics for four different comparisons are given in Table 2. The full sample distributions are statistically significantly different for the coefficients for the first three eigenvectors and different for all four eigenvectors for the two populations of FeLoBALQs.

FeLoBALQs are characterized by larger (smaller) velocity offsets and broader (narrower) lines.

The differences between the SPCA coefficients among the different classes is profound. Some dependences are expected because $E1$ and SPCA coefficient 1 both measure the inverse relationship between the Fe II and [O III] emission. Other dependencies are more subtle. For example, for $E1 > 0$ FeLoBALQs, SPCA coefficient 2 is almost never negative. This result means that this eigenvector, characterized by a negative-flux narrow Hβ line, serves to broaden and reduce the flux of the Hβ line in this subclass. It is also interesting that the coefficients of the first eigenvector are sufficient to distinguish between the $E1$ subgroups of the comparison sample; the remaining three are identical for the $E1$ subgroups for the comparison sample but not for the FeLoBALQs. This result demonstrates the tight relationship between the $E1$ parameter and SPCA1.

The distribution of $L_{\rm Bol}$ is seen in Figure 8. It is notable that the comparison sample $L_{\rm Bol}$ distributions split at $E1 = 0$ are consistent, but the FeLoBALQ sample $L_{\rm Bol}$ distributions for $E1 > 0$ and $E1 < 0$ are significantly different ($p < 0.001$; Table 1). The median values for the $E1 < 0$ and $E1 > 0$ FeLoBALQs are 45.9 and 46.5. The relationship between $E1$ and $L_{\rm Bol}$ is shown in Figure 11. Recalling that the FeLoBALQs were chosen based solely on their spectroscopic classification, this result seems to be surprising and seems to represent a fundamental property of low-redshift FeLoBALQs.

The black hole mass in the $E1 > 0$ FeLoBALQs is lower than in the $E1 < 0$ FeLoBALQs, but no such significant difference is present among the comparison objects. Recall that the black hole mass estimate depends on luminosity and Hβ line width so that more luminous objects with broader lines have larger black hole masses. In our case, the $E1 > 0$ ($E1 < 0$) objects have narrower (broader) Hβ lines and larger (smaller) luminosities so that one might expect that the $E1 > 0$ and $E1 < 0$ objects should have more or less the same black hole mass distribution. The differences in luminosity and black hole mass are propagated into $L_{\rm Bol}/L_{\rm Edd}$, with the $E1 < 0$ FeLoBALQs accreting at rates more than half a dex lower than the $E1 > 0$ FeLoBALQs. This difference seems to be a fundamental one and an identifying feature of the two groups of FeLoBALQs.

Despite the differences in the black hole mass and Eddington ratio distributions, the size of the 2800 Å continuum emission region is the same for the $E1 < 0$ and $E1 > 0$ objects. The emission region size depends on the temperature distribution as

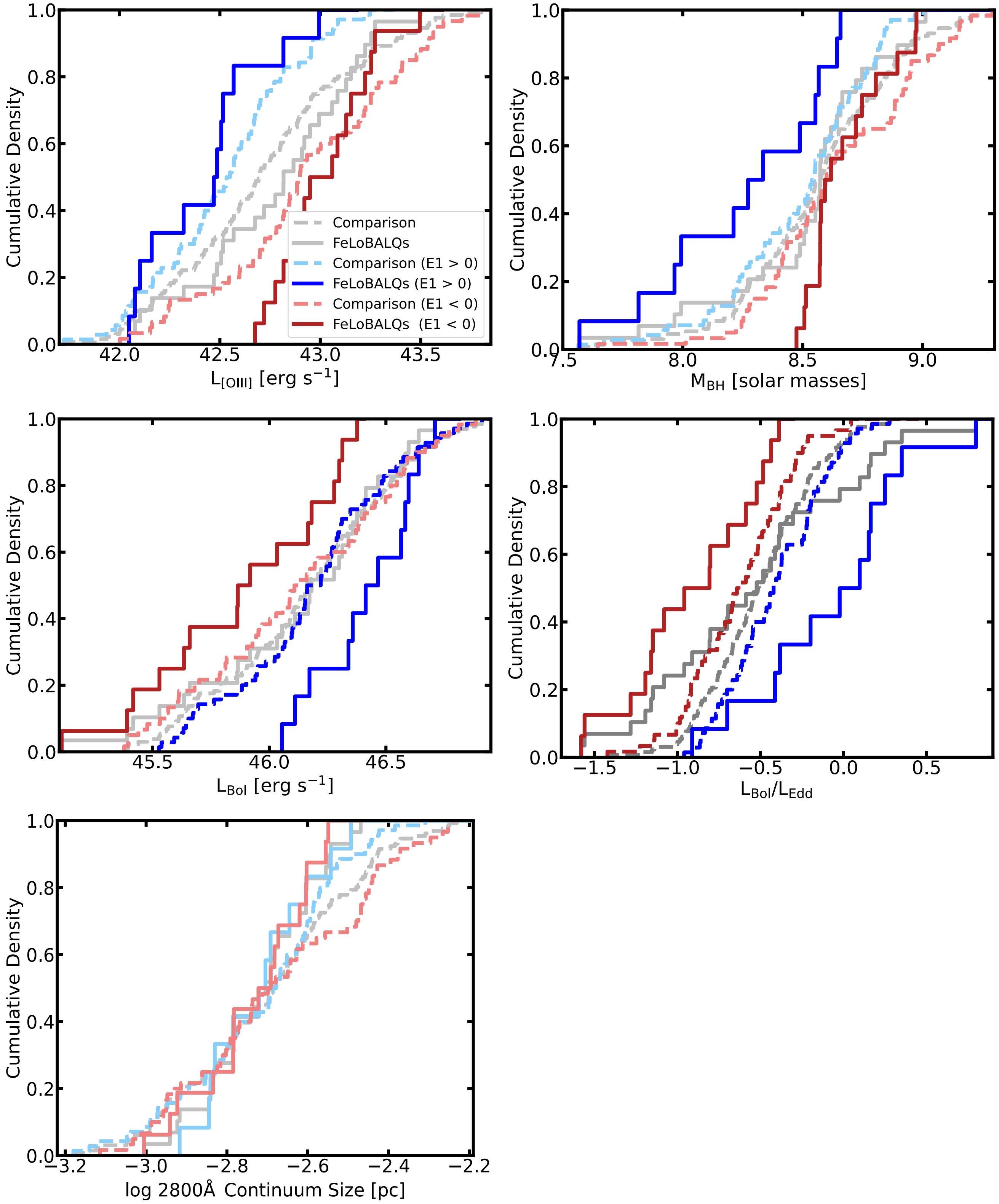

Figure 8. Cumulative distribution plots of the global properties: the integrated [O III] luminosity, bolometric luminosity, black hole mass (computed as described in Section 2.2), Eddington ratio $L_{\rm Bol}/L_{\rm Edd}$, and size of the 2800 Å continuum emission region. The distributions are consistent between the FeLoBALQs and comparison sample for most of these properties; the exception is the A-D detection of a difference in the Eddington ratio. However, the two $E1$-parameter classes of FeLoBALQs are significantly different for the first four parameters.

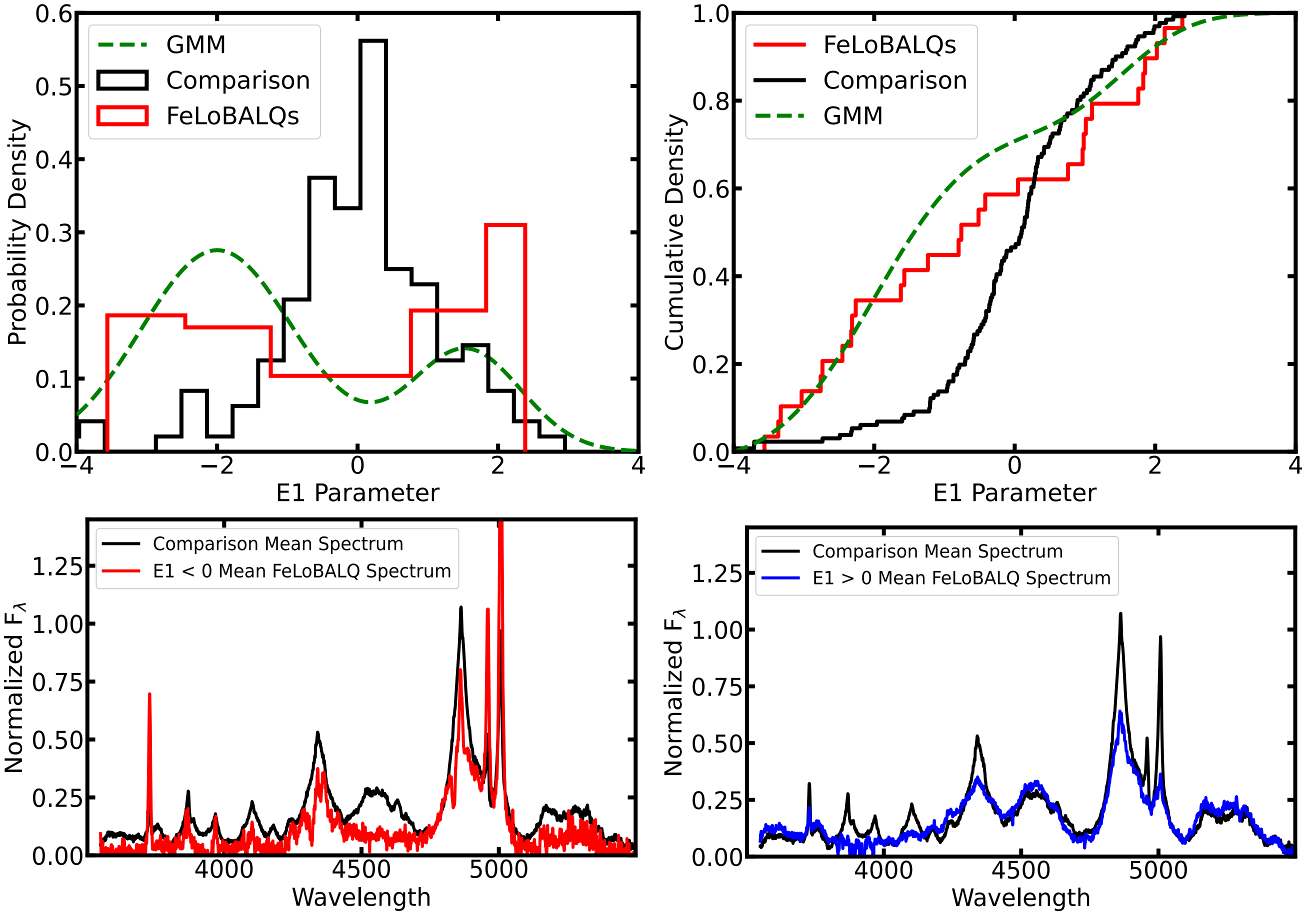

Figure 9. The distribution of the *E*1 parameter for the FeLoBALQs is different than for the comparison sample. Top: histogram of the *E*1 parameter (left) and the cumulative distribution (right). Both plots show that there is an excess of FeLoBALQs at both low and high *E*1 parameters. The dashed green line shows the two-component GMM for the FeLoBALQs. Bottom: weighted mean spectra of the FeLoBALQs with an *E*1 parameter of less than zero (left) and greater than zero (right), both compared with the weighted mean spectrum from the comparison sample. The objects with $E1 < 0$ are characterized by stronger [O III] and weaker Fe II than the mean comparison sample spectrum, while objects with $E1 > 0$ are characterized by weaker [O III] and weaker Balmer lines than the mean comparison sample spectrum.

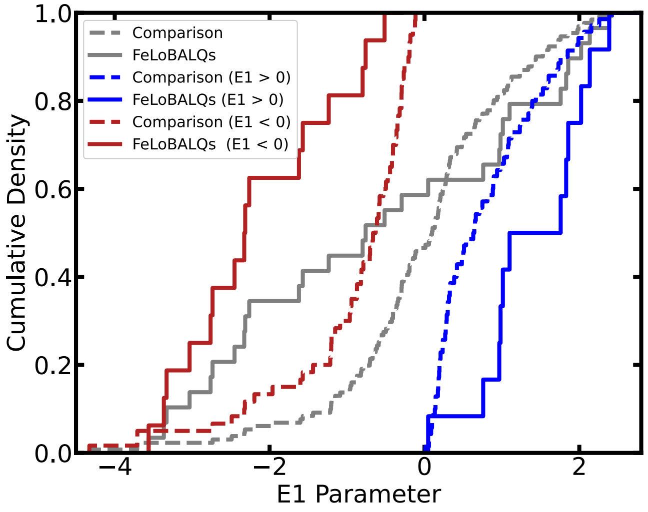

Figure 10. Cumulative distributions of the *E*1 parameter. The FeLoBALQs and comparison sample show dramatically different distributions, both for the whole sample and for the samples divided by positive and negative *E*1.

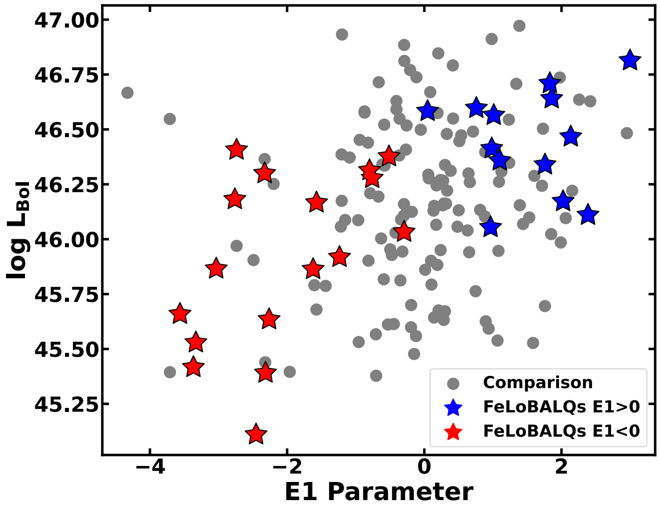

Figure 11. Bolometric luminosity as a function of the *E*1 parameter. The distribution of the bolometric luminosity for the comparison sample is approximately normal, with no preference for *E*1 (Figure 8), while the $E1 > 0$ ($E1 < 0$) FeLoBALQs have a higher (lower) $L_{\rm Bol}$ than average.

a function of radius. The radius for a particular temperature should be larger for a larger accretion rate and black hole mass. The black hole mass is larger (smaller) for the $E1 < 0$ ($E1 > 0$) objects, but the accretion rate is smaller (larger), so the two effects cancel out.

3.4. Spearman Rank Correlations

The 17 optical emission line and global properties were correlated against one another for both the FeLoBALQ and comparison samples (Figure 12). The Spearman rank correlation is appropriate for these nonparametric data. The plots represent the log of the p-value for the correlation, where the sign of the value gives the sense of the correlation. That is, a large negative value implies a highly significant anticorrelation.

Our method for propagating errors is described in Section 2.2. We chose $p < 0.05$ as our threshold for significance. The overplotted stars show the fraction of draws that yield p-values greater than our threshold value. Generally, taking the errors into account did not affect the significance of a correlation, if present.

As discussed in Section 3, correlations among quasar properties associated with the Boroson & Green (1992) eigenvector 1, here parameterized using the $E1$ parameter, dominate and potentially obscure other correlations. We would like to determine whether there were correlations independent of the $E1$ parameter. It is also possible that the two classes of FeLoBALQs show different correlation behaviors that would be washed out in the whole-sample correlations. Therefore, we also compute the Spearman rank correlation coefficient between the parameters divided by $E1 < 0$ and $E1 > 0$ (Figure 12, middle and bottom panels).

Some of the correlations we observe are a consequence of parameter dependence. Other correlations are very well known, for example, the anticorrelation between $R_{\mathrm{Fe\,II}}$ and the [O III] equivalent width. The origin of these correlations has been discussed exhaustively in the literature (e.g., Shen & Ho 2014, and references therein). Notable correlations and other patterns in the data are discussed in the sections below.

As discussed in Section 2.2, the [O III] and Fe II emission is weak in some objects, and it is possible to consider the measurements of those variables that are not found to be significant using the F-test to be upper limits. The generalized Kendall tau test can be used for censored data (Isobe et al. 1986). We use the `pymccorrelation` implementation (Privon et al. 2020) on the [O III] equivalent width, $R_{\mathrm{Fe\,II}}$, and [O III] luminosity and looked for parameter combinations that either switched from being a significant correlation ($P < 0.05$) to insignificant or vice versa. For the FeLoBALQs 13 correlations (9% of the 144 nontrivial correlations for these three parameters) changed, with four becoming insignificant and nine becoming significant. For the comparison sample, 12 correlations (8%) changed, with four becoming insignificant and eight becoming significant. We credit these minor changes to the fact that the upper limits only strengthen the observed anticorrelation between [O III] and $R_{\mathrm{Fe\,II}}$ that defined $E1$ because [O III] (Fe II) was found to be statistically unnecessary only among the $E1 > 0$ ($E1 < 0$) objects.

3.4.1. Shen & Ho 2014

Shen & Ho (2014) presented an analysis of ∼20,000 low-redshift quasars from the SDSS DR7 quasar catalog. They asserted that $R_{\mathrm{Fe\,II}}$ is a measure of the accretion rate relative to the Eddington value (the Eddington ratio), with large values of this parameter corresponding to a large Eddington ratio. They found a wide range of values of the Hβ FWHM for a given value of $R_{\mathrm{Fe\,II}}$ and suggested that the dispersion of the Hβ FWHM for a given value of $R_{\mathrm{Fe\,II}}$ reflects a range of viewing angle orientations to a disklike broad-line region.

We reproduced their Figure 1 for the FeLoBALQs and comparison sample in the left panel of Figure 13. We already know from Section 3.2.1 and Figure 6 that the Hβ FWHM is systematically broader among the FeLoBALQs. This representation shows that the difference is a function of $R_{\mathrm{Fe\,II}}$ such that objects with larger (smaller) values of $R_{\mathrm{Fe\,II}}$ have systematically smaller (larger) Hβ FWHM. We highlight the difference by computing the median value in bins of $R_{\mathrm{Fe\,II}}$ such that each bin has the same number of points: six bins of 22 objects each for the comparison sample and three bins of 10 objects each for the FeLoBALQs.

To quantify the difference, we defined a parameter called the Hβ FWHM deviation, abbreviated hereafter as deviation. To compute the deviation for each point, we first linearly interpolated the medians computed above for the comparison sample. For points with larger $R_{\mathrm{Fe\,II}}$ values than the median of the largest or smallest bin, we used the two nearest median points to extrapolate. The deviation was then defined to be the difference between the log of the observed Hβ FWHM and the log of the interpolated relationship. Shen & Ho (2014) found a lognormal distribution of Hβ FWHM as a function of $R_{\mathrm{Fe\,II}}$ with a dispersion of 0.15–0.25 dex. The dispersion in the deviation for the comparison sample is 0.18 and thus consistent with the Shen & Ho (2014) value.

The cumulative distribution of the deviation is shown in Figure 13. It is useful to compare this plot with the Hβ FWHM cumulative distribution (Figure 6). The median values of FWHM for the $E1 < 0$ and $E1 > 0$ groups are dramatically different. This result is now explained because the two groups are characterized by much different values of $R_{\mathrm{Fe\,II}}$, since $R_{\mathrm{Fe\,II}}$ contributes to the definition of the $E1$ parameter. The deviation parameter takes this difference into account because it is a function of $R_{\mathrm{Fe\,II}}$. The cumulative distributions show that the median deviation for the comparison sample is consistent with zero (by definition), and the median value for the FeLoBALQs is 0.17, corresponding to a 47% systematically larger Hβ FWHM when averaged over all of the objects.

Shen & Ho (2014) conjectured that the deviation in Hβ FWHM at each value of $R_{\mathrm{Fe\,II}}$ is a consequence of differences in orientation. If true, our result implies that the FeLoBALQs are observed at systematically larger inclination angles than objects without absorption. If we take the effective mean inclination with respect to the normal of unabsorbed objects to be 30° (e.g., Shen & Ho 2014), then assuming the same geometry for the broad-line region and a $\sin\theta$ dependence, we find that the effective mean inclination to the broad-line quasars should be 48°. The FWHM enters the virial black hole mass as FWHM^2, so a 47% larger value suggests that the black hole masses for the FeLoBALQs are overestimated by a factor of 2.2, on average.

A larger-inclination viewing angle might be expected for BALQs. Due to the requirement that angular momentum be dispersed for accretion to occur, the accreting gas is expected to be disklike, not only at the smallest scales (i.e., the optical-UV emitting accretion disk) but also at larger scales (the molecular torus and beyond). If that material is transported perpendicular

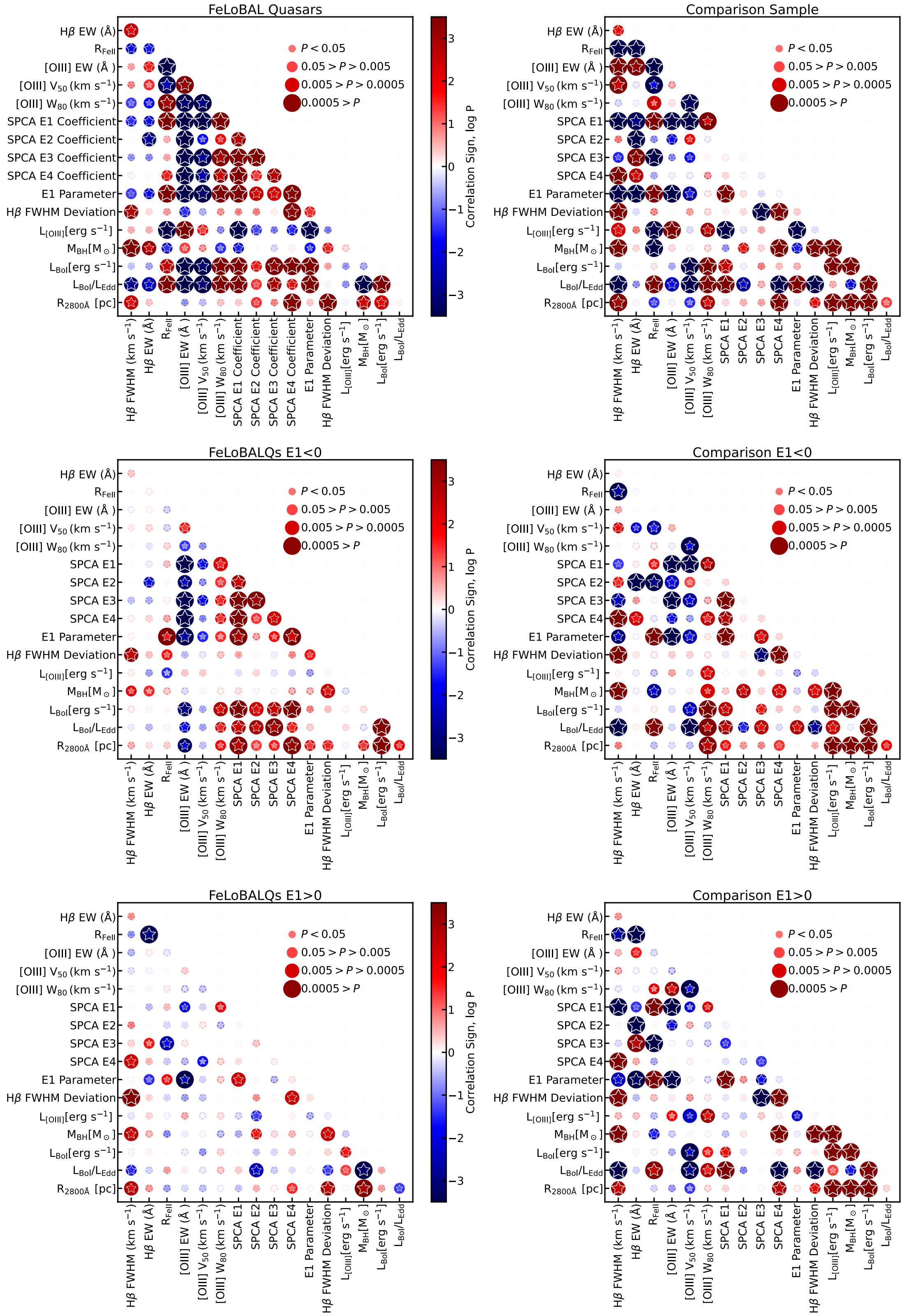

Figure 12. Results of the Spearman rank correlation analysis for the FeLoBALQs (left) and comparison sample (right). The size and color of the marker indicate the sign and *p*-value of the correlation. Anticorrelations are shown in blue, and correlations are shown in red. The saturation of the color indicates the significance of the correlation as a continuous variable, while the discrete sizes of the points characterize a range of *p*-values as shown in the legend. The circles show the results for parameter values. The stars show the results for a Monte Carlo scheme to estimate the effects of the errors (see text for details). The top panels show the results for all 30 FeLoBALQs and 132 comparison sample objects, while the bottom panels show the results divided by the *E*1 parameter. Many parameters show similar correlations in both panels; however, some expected correlations, for example, between the bolometric and [O III] luminosities, are missing in the FeLoBALQ sample.

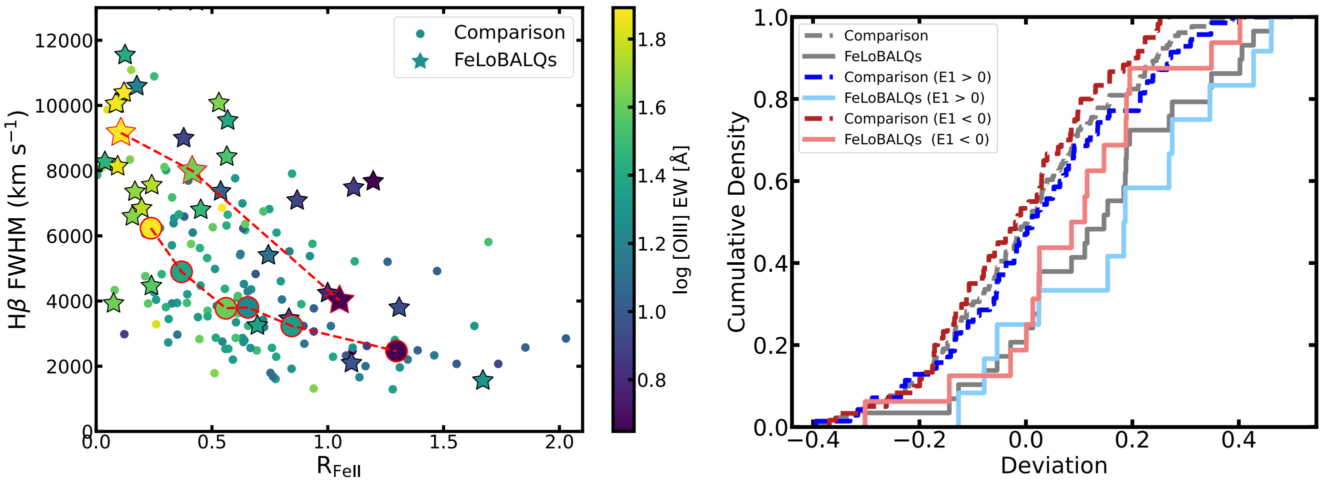

Figure 13. Left: Hβ FWHM as a function of $R_{\rm Fe\,II}$ for the FeLoBALQs and comparison sample following Shen & Ho (2014). The large points outlined in red show the median Hβ FWHM values in bins of $R_{\rm Fe\,II}$. It is clear that the Hβ FWHM is systematically broader in the FeLoBALQs for a given value of $R_{\rm Fe\,II}$. Right: cumulative distributions of the deviation parameter. The color scheme is the same as that in Figure 6. The deviation parameter separates the FeLoBALQs from the unabsorbed comparison sample more cleanly than does the Hβ FWHM (Figure 6).

to the disk by some local mechanism (i.e., radiative line driving, scattering on dust), then, once the material rises sufficiently to be illuminated by the brilliant quasar nucleus, the stream lines should be bent radially so that the observer views the quasar nucleus through absorbing gas only along certain lines of sight (e.g., Elvis 2000).

Although promising, a larger-inclination viewing angle falls short of explaining all of the differences between the FeLoBALQs and the comparison sample. For example, it does not explain the FeLoBALQ $E1$ bimodality. Moreover, the explanation is not unique. A broader Hβ emission line would also be produced if the broad-line region were truncated at its outer boundary. Quasars with double-peaked broad lines are extreme examples of such objects (e.g., Strateva et al. 2003), and Fe II absorption has been found in several (Halpern et al. 1996; Halpern 1997; Eracleous et al. 2003). We favor this interpretation and will return to this idea in Paper IV (Leighly et al. 2022, in preparation).

3.4.2. Boroson 2002

Boroson & Green (1992) presented a principal component analysis of measured emission line and continuum properties near Hβ in a sample of 87 low-redshift quasars from the Bright Quasar Survey (Hewett et al. 1995). Boroson (2002) used these results augmented by results from a sample of radio-loud objects to investigate the role of the PCA eigenvectors in determining an object's class, i.e., whether an object is radio-loud or radio-quiet. His sample included a small number of BALQs. His discussion culminates in his Figure 7, an interpretive diagram that used principal components 1 and 2 to classify AGNs and quasars.

We present a similar analysis to determine whether the same pattern of behavior is present among our FeLoBALQs and the comparison sample. The difference is that we used the coefficients derived from model fitting using the spectral principal component analysis eigenvectors created from the comparison sample (Section 2.3). The PCA eigenvector coefficients are invariant under sign change, so we use the composite spectra shown in Boroson (2002, Figure 2) to orient ours. The results are shown in Figure 14. The negative of our SPCA1 coefficients corresponds well with the Boroson (2002) PC1 coefficients. The SPCA2 coefficients correspond less well with the Boroson (2002) PC2 coefficients, so we used the [O III] equivalent width in the composite spectra to assign the negative of our SPCA2 coefficients to the Boroson (2002) PC2 coefficients. Figure 14 (middle) shows the SPCA2 eigenvector coefficients as a function of the SPCA1 eigenvector coefficients. To make the plot more similar to Figure 1 in Boroson (2002), the SPCA coefficients were scaled by dividing by the standard deviation of the comparison sample in each quadrant. The FeLoBALQ coefficients are also plotted; their SPCA values have been scaled with the same factors as the comparison sample.

This figure highlights some interesting differences between the comparison objects and the FeLoBALQs. There is a striking difference between comparison and FeLoBALQ number density in the left two quadrants. The upper left quadrant includes 30% of the comparison objects but only one FeLoBALQ, while the lower left quadrant includes 40% of the FeLoBALQs but only 11% of the comparison objects. Thus, there is a strong difference in SPCA2 between the comparison objects and the FeLoBALQs. Examining the composite spectra in the left two panels in Figure 14 and the PCA eigenvectors in Figure 4 shows that the difference is that the FeLoBALQs have weaker and broader Balmer emission lines, a property that should correlate with SPCA2. As noted above, a physical interpretation of this result is not obvious.

Boroson (2002) used his Figure 1 and the ensuing discussion to construct a schematic interpretive diagram based on PC1 and PC2 (his Figure 7). He argued that PC1 is a measure of the Eddington ratio, and PC2 is a measure of the accretion rate, which is equivalent to the luminosity for a constant accretion efficiency. Lines of constant black hole mass lie along the diagonal. He found that a plot of PC2 versus PC1 distinguishes between radio-loud and radio-quiet quasars. He concluded that narrow-line Seyfert 1 galaxies and BALQs (both generally radio-quiet) are characterized by high values of the Eddington ratio, with the BALQs additionally characterized by a high accretion rate. Radio-loud objects have larger black hole masses and lower accretion rates.

Comparing the middle panel of Figure 14 with Boroson's (2002) Figure 7 shows that the density of BALQs in our sample is

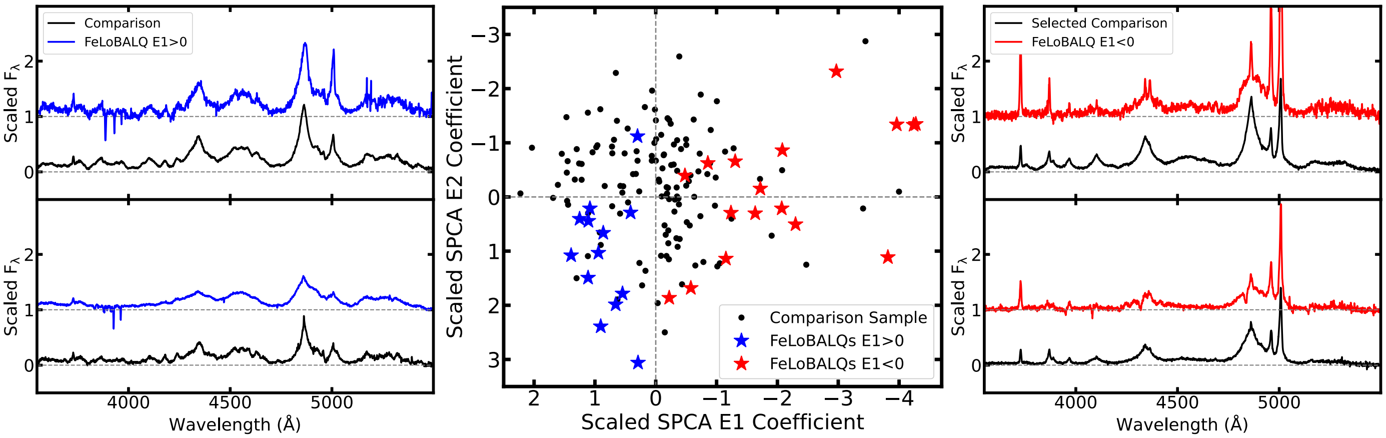

Figure 14. Plots modeled after Figures 1 and 2 in Boroson (2002). The middle panel shows the spectral PCA fit coefficients scaled by the variance of the comparison sample in each quadrant. The right and left panels show weighted mean composite spectra from each quadrant offset in the *y*-direction for plot clarity. The highest concentration of FeLoBALQs relative to comparison objects is found in the lower left quadrant, as predicted by Boroson (2002); however, all of the $E1 < 0$ objects lie in the two right quadrants, where Boroson (2002) found radio-loud quasars.

high in the lower left quadrant, as predicted. A difference is that all of the $E1 < 0$ FeLoBALQs lie on the right side of the diagram, as they should, since $E1$ is strongly correlated with the SPCA1 coefficient. The right side of the diagram is where the Boroson (2002) radio-loud objects are. Some of our FeLoBALQs may be radio-loud; a systematic investigation of the radio properties of this sample is beyond the scope of this paper. However, we note that SDSS J102226.70+354234.8 has a resolved two-sided jet and $E1 = 0.97$, and SDSS J164419.75+530750.4 has a 500 kpc scale radio lobe with bilateral hot spots and $E1 = -0.51$ (L. Morabito 2021, private communication).

Because we have measured the Eddington ratio and can compute the accretion rate, we can directly investigate whether our principal component coefficients correlate with these properties and render the Boroson (2002) Figure 7 using our measurements (Figure 15). As shown in Figure 12, SPCA1 is strongly positively correlated with the Eddington ratio (comparison: $p = 6.4 \times 10^{-10}$; FeLoBALQs: $p = 3.2 \times 10^{-8}$). The accretion rate was computed using $L_{\rm Bol} = \eta \dot{M} c^2$, where we assumed a constant $\eta = 0.1$, acknowledging that this value may not be accurate at very low or very high accretion rates. The accretion rate is strongly correlated with the SPCA1 coefficients (comparison: $p = 0.0022$; FeLoBALQ: $p = 1.1 \times 10^{-6}$). It is not strongly correlated with SPCA2 (comparison: $p = 0.6$; FeLoBALQ: $p = 0.014$). Thus, the *x*-axis in our figure and Boroson's (2002) Figure 7 both correspond to the first eigenvector; this is further illustrated by the color bar corresponding to the $E1$ parameter value in Figure 15. However, our *y*-axis does not correspond with the second eigenvector. So, although we assigned SPCA2 to the *y*-axis in Figure 14 based on the features in the composite spectra, we did not find that SPCA2 is a measure of the accretion rate, although it does very well separate the $E1 > 0$ FeLoBALQs from the comparison objects.

In addition, Figure 15 shows that in our sample, the FeLoBALQs and comparison sample objects are distributed roughly uniformly in Eddington ratio versus accretion rate space (although statistically distinguishable; see Figures 9 and 10 and Table 2) and are not relegated to high Eddington ratios and accretion rates, as proposed by Boroson (2002).

We note that other recent work in the UV rest wavelengths does not support the classification scheme proposed by Boroson (2002). There is evidence that the blueshift and equivalent width of the C IV emission line are associated with the Boroson & Green (1992) eigenvector 1 (e.g., Wills et al. 1999; Shang et al. 2003) and therefore, by extension, the Eddington ratio. Rankine et al. (2020) found that BALQs exist throughout C IV blueshift/equivalent width space, and Rankine et al. (2021) showed that radio-loud quasars similarly populate this space. We used Boroson (2002) for our discussion because he used the rest-frame optical eigenvectors and is therefore more similar to our analysis.

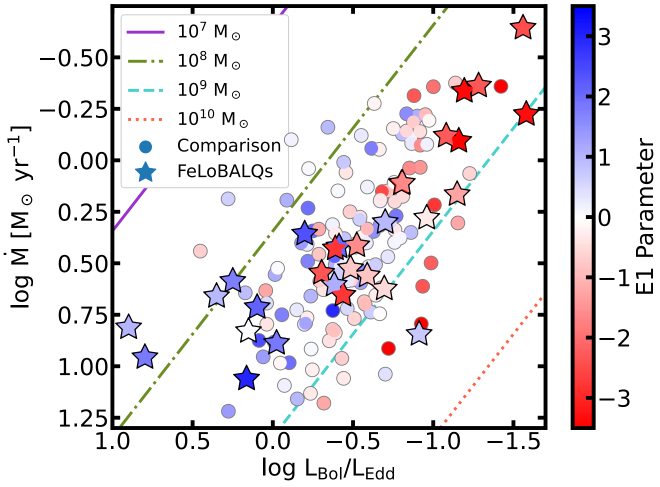

Figure 15. Plot modeled after Figure 7 in Boroson (2002) rendered using our estimates of the Eddington ratio and accretion rate. Boroson (2002) predicted that BALQs should lie in the lower left corner of this plot, i.e., high Eddington ratio. We found that the FeLoBALQs are characterized by both low and high Eddington ratios, although their distribution in this parameter is statistically different from the distribution of the comparison objects; see Figures 9 and 10 and Table 2.

3.4.3. Correlations among Global Properties

Next, we examined correlations among the global parameters: the black hole mass, bolometric luminosity, and accretion rate relative to Eddington.

We found that the $E1$ parameter is strongly positively correlated with $L_{\rm Bol}$ among the FeLoBALQs ($p = 4.4 \times 10^{-5}$), but no such correlation is present in the comparison sample

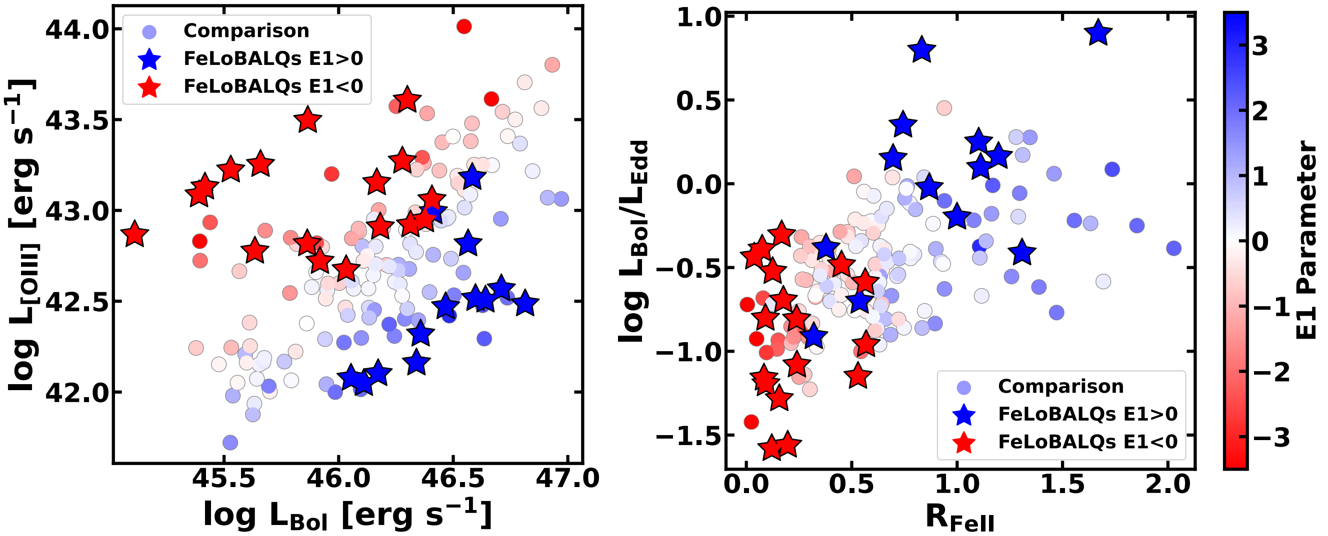

Figure 16. Relationships among global parameters. In the left panel, a strong positive correlation is observed between the bolometric and [O III] luminosity for the comparison sample ($p = 5.2 \times 10^{-19}$) but not for the FeLoBALQs ($p = 0.12$). Rather, they form two rough tracks of approximate correlation on either side of the comparison sample objects and divided by the $E1$ parameter. Right: computed ratio of the bolometric to Eddington luminosity as a function of $R_{\rm Fe\ II}$. The two parameters are correlated ($p = 1.2 \times 10^{-4}$ for the FeLoBALQs, and $p = 7.1 \times 10^{-11}$ for the comparison sample).

($p = 0.15$). This result echoes Figure 11, which shows that the $E1 < 0$ FeLoBALs are less luminous than the $E1 > 0$ FeLoBALs (Section 3.3). Thus, the optical spectral properties of FeLoBALQs in this sample predict the luminosity. This result is surprising and unexpected.

We also investigated the [O III] luminosity. There is a correlation between the bolometric and [O III] luminosity in the comparison sample ($p = 5.2 \times 10^{-19}$). This type of correlation is expected in a flux-limited sample. The interesting fact is that no correlation is found between these parameters for the FeLoBALQs ($p = 0.12$). Figure 16 shows the reason for this behavior. While the correlation in the comparison sample is clearly seen, the FeLoBALQs instead form two (or more) clumps on either side of the comparison sample regression. This behavior further underlines the presence of two types of FeLoBALQs in this sample.

The $R_{\rm Fe\ II}$ parameter can be taken as a proxy for the accretion rate relative to Eddington (e.g., Shen & Ho 2014). Figure 16 shows the relationship between these two parameters. A correlation exists, but it is rough, although statistically significant for both the FeLoBALQs and the comparison sample ($p = 1.2 \times 10^{-4}$ and 7.1×10^{-11}, respectively). Why are these two parameters not perfectly correlated? Several approximations enter into the computation of $L_{\rm Bol}/L_{\rm Edd}$. The $L_{\rm Edd}$ depends on the black hole mass. The black hole mass was estimated using the FWHM of the Hβ line and following the formalism of Collin et al. (2006). In particular, we used their Equation (7) to estimate the scale factor f based on the FWHM of the Hβ line. This assumption must be a simplification given the systematically broader Hβ lines observed among the FeLoBALQs, whether that property originates in a more inclined viewing angle or a lack of a traditional broad-line region component (or both). If the origin of the broader Hβ lines is viewing angle inclination, then the simplification would bias the black hole masses larger than they should be. Also, we used the measured L_{5100} luminosity to compute the radius of the broad-line region without correcting for reddening. A too-small $R_{\rm BLR}$ would bias the black hole mass smaller than it should be.

The bolometric luminosity was computed using a bolometric correction factor from the 3 μm luminosity density (Gallagher et al. 2007). That bolometric correction factor was computed from relatively luminous quasars that typically show near-infrared emission from a torus. Thus, objects that are weak at 3 μm will potentially have underestimated bolometric luminosities. In Paper IV, we will investigate the optical-to-IR SED and find that some $E1 < 0$ objects are weak at 3 μm.

The combination of uncertainties in the black hole mass and bolometric luminosity estimates must contribute to the scatter in $L_{\rm Bol}/L_{\rm Edd}$ seen in the right panel of Figure 16. It is interesting that among the $E1 < 0$ FeLoBALQs, $L_{\rm Bol}/L_{\rm Edd}$ is correlated with $L_{\rm Bol}$ but not $M_{\rm BH}$ ($p = 5.6 \times 10^{-6}$ and 0.36, respectively), while the opposite is true for the $E1 > 0$ FeLoBALQs ($p = 0.18$ and 1.2×10^{-4}, respectively; Figure 12). It is possible that, in this sample, $R_{\rm Fe\ II}$ better reflects the physical conditions of the nucleus anticipated to depend on accretion rate than does the computed value of $L_{\rm Bol}/L_{\rm Edd}$. It would be interesting to obtain stellar velocity dispersion black hole estimates to substantiate this inference.

A related question is, how interchangeable are $E1$, the first SPCA coefficient, $R_{\rm Fe\ II}$, and the Eddington ratio? All of these parameters are highly correlated (Figure 12); the largest p-value among all six combinations is 1.2×10^{-4} (9.3×10^{-7}) for the FeLoBALs (comparison sample). Yet the $E1$ parameter is the only one of the four that passes the GMM test for bimodality (Section 3.3), i.e., a distribution with negative kurtosis and a better fit with two heteroskedastic Gaussian distributions than with one, even though bimodality is not convincingly established, since the distribution fails the nonparametric dip test. At least $R_{\rm Fe\ II}$ and the Eddington ratio have distributions with negative kurtosis. Perhaps these differences imply that the $E1$ parameter captures an essence of the data that is blurred among the other parameters.

4. Discussion and Conclusions

We present an analysis of the rest-optical spectra near Hβ of a unique sample of low-redshift ($z < 1$) FeLoBALQs. All objects have sufficient quality data that the Hβ/[O III] region of the spectrum could be analyzed. Many of the objects were selected using a convolutional neural net (C. Dabbieri et al. 2022, in preparation) applied to $0.8 < z < 1$ quasars from the DR14 quasar catalog (Pâris et al. 2018), and of the 30 objects, 11 had not been classified as a BALQ previously. A 132-object comparison sample, matched in redshift, median S/N in the Hβ region, and 3 μm luminosity density, was compiled and analyzed in parallel.

BALQs can be difficult to find and recognize compared with unabsorbed quasars; therefore, construction of a uniform sample is difficult. The SDSS quasar catalogs require the presence of a broad emission line in the spectrum and therefore can be biased against heavily absorbed quasars; for example, the spectacular FeLoBALQ SDSS J135246.37+423923.5 (Choi et al. 2020) is not in the DR14 quasar catalog. However, our selection process reduces some of the pitfalls of other samples. Although the sample is not large, it is larger than any samples of rest-frame Hβ-region spectra of BALQs considered to date (Yuan & Wills 2003; Runnoe et al. 2013; Schulze et al. 2017; 16, 8, and 22 objects, respectively). The sample may be more homogeneous, since we chose only FeLoBALQs. BALQ properties such as outflow velocity show strong luminosity dependence (e.g., Laor & Brandt 2002; Ganguly et al. 2007). Because our sample spans only a small range of redshift, the range of luminosities is small. The SDSS spectra have more uniform quality than the near-infrared spectra can due to variable-quality telluric correction and other factors, such as fixed pattern noise, that degrade the spectra. The ability to compile a large and uniform comparison sample that could be analyzed uniformly turned out to be critical for many of the conclusions in the paper.

Our analysis focused on measurement of the Hβ, [O III], and Fe II. We used traditional multicomponent model fitting, as well as a principal component analysis. We found that the variance in the emission lines in the comparison sample was principally associated with the Boroson & Green (1992) eigenvector 1, as expected. We defined an empirical parameter $E1$, which is a function of the [O III] equivalent width and $R_{\rm Fe\,II}$, the ratio of the Fe II emission to the Hβ emission (e.g., Shen & Ho 2014). Both $E1$ and $R_{\rm Fe\,II}$ were found to be strongly correlated with the Eddington ratio (Figures 12 and 16). A large and positive $E1$ parameter corresponds to a high Eddington ratio, while a large and negative $E1$ parameter corresponds to a low Eddington ratio.

The large and well-defined matched sample of unabsorbed quasars allowed us to test whether low-redshift FeLoBALQs have the same rest-frame optical emission line properties as unabsorbed objects. The principal result of the paper is that they do not. The unabsorbed quasars have a peaked distribution in the $E1$ parameter (Figure 9). In contrast, the FeLOBALQs show an apparent bimodal distribution in $E1$. Moreover, the luminosities of the two groups of FeLOBALQs is different (Figures 8 and 11), and those differences carry over to a difference in Eddington ratio (Figure 8). The implication is that the low-redshift FeLoBALQs are characterized by either a large Eddington ratio or a small one but not an intermediate value. This division is echoed in the relationship between [O III] and $L_{\rm Bol}$. These parameters are correlated in the comparison sample but clustered by $E1$ in the FeLoBALQs (Section 3.4.3; Figure 16).

This result is new and distinct from what has been previously reported in the literature. Less work has been done in the rest-frame optical band compared with the rest-frame UV; nevertheless, it has been reported either that BALQs appear to be high Eddington ratio objects (Yuan & Wills 2003; Runnoe et al. 2013) or that there is no difference between absorbed and unabsorbed objects (Schulze et al. 2017). The difference between our results and the previous ones likely stems from the large and uniform parent sample: the low-redshift SDSS quasar catalog, supplemented by FeLoNET, our convolutional neural net, used to discover one third of the FeLoBALQs analyzed here. This result inspires a question: why does FeLoBAL absorption occur in objects with high and low accretion rates but not in objects with an intermediate accretion rate? This question will be addressed in Paper IV (Leighly et al. 2022, in preparation).

We found that the measurements of the Hβ FWHM of the FeLoBALQs are consistently larger than those of the comparison sample (Figure 6). Moreover, they are consistently larger for the same value of $R_{\rm Fe\,II}$ (Section 3.4.1; Figure 13). Shen & Ho (2014) proposed that $R_{\rm Fe\,II}$ corresponds to the Eddington ratio, and that the scatter in Hβ width indicates objects with different inclination angles. If this interpretation is correct for the FeLoBALQs, then, if normal quasars are typically observed at 30° from normal to the accretion disk, the FeLoBALQs are typically observed at 48°. However, this reasoning does not explain all of the many differences we found between the FeLoBALQs and the unabsorbed comparison sample; for example, it does not explain the apparent bimodality in the FeLoBAL distribution. Moreover, this explanation is not unique. Instead, the narrow core of the Hβ emission line may be missing. Additional support for this idea will be presented and discussed in Paper IV (Leighly et al. 2022, in preparation).

We compared our results with those of Boroson (2002). He found evidence that the rest-frame optical-band PCA eigenvector coefficients could be used to separate quasars among narrow-line Seyfert 1 galaxies, BALQs, and radio-loud objects. In particular, he found that the BALQs were relegated to a corner of the PCA1–PCA2 coefficient graph. We confirmed that nearly all of our $E1 > 0$ (high Eddington ratio) FeLoBALQs fell in that region of parameter space. However, we found that all of our $E1 < 0$ were scattered among the radio-loud objects in the Boroson (2002) scheme. We are in the process of investigating the radio properties of this sample. We also note that more recent work using rest-frame UV spectra has found a more uniform distribution of types of objects (e.g., Rankine et al. 2020, 2021).

Moving forward, we note that the Fe II absorption spectrum blankets the rest-frame UV region, and FeLoBALQs can be observed to redshifts higher than $z \sim 3$. In a flux-limited sample like the SDSS, higher-redshift samples are comprised of higher-luminosity objects. Assuming a fixed Eddington ratio distribution, such objects will have larger black hole masses. A larger black hole mass will have a softer (UV-dominant) SED, which could affect the outflow in two ways. The softer SED might produce an outflow with a different ionization balance, i.e., a larger fraction of lower-ionization species, which means the observed absorption could change. A dramatic change is probably not expected; the observed absorption lines should depend principally on the ionization parameter, as is usually the case. The softer SED should be more efficient in accelerating outflows, since it has more photons with wavelengths suitable for resonance scattering and fewer likely to overionize the outflowing gas. In fact, we see some evidence for faster outflows and shifted parameters among the higher-redshift FeLoBALQs we have analyzed already (Voelker et al. 2021). We also expect that lower Eddington ratio objects will be rarer (e.g., Jester et al. 2005). This is because the black hole mass function is steep, and objects with black holes larger than $10^{10}\,M_\odot$ are very rare.

K.M.L. acknowledges very useful conversations with Leah Morabito and thanks Alex Parsells for running the Hartigan & Hartigan (1985) dip test. Support for SimBAL development and analysis is provided by NSF Astronomy and Astrophysics grant Nos. 1518382, 2006771, and 2007023. This work was performed in part at the Aspen Center for Physics, which is supported by National Science Foundation grant PHY-1607611. S.C.G. thanks the Natural Science and Engineering Research Council of Canada.

Long before the University of Oklahoma was established, the land on which the university now resides was the traditional home of the "Hasinais" Caddo Nation and "Kirikiris" Wichita & Affiliated Tribes. This land was also once part of the Muscogee Creek and Seminole nations.

We acknowledge this territory once also served as a hunting ground, trade exchange point, and migration route for the Apache, Comanche, Kiowa, and Osage nations. Today, 39 federally recognized tribal nations dwell in what is now the State of Oklahoma as a result of settler colonial policies designed to assimilate Indigenous peoples.

The University of Oklahoma recognizes the historical connection our university has with its Indigenous community. We acknowledge, honor, and respect the diverse Indigenous peoples connected to this land. We fully recognize, support, and advocate for the sovereign rights of all of Oklahoma's 39 tribal nations.

This acknowledgment is aligned with our university's core value of creating a diverse and inclusive community. It is our institutional responsibility to recognize and acknowledge the people, culture, and history that make up our entire OU Community.

Funding for the SDSS and SDSS-II has been provided by the Alfred P. Sloan Foundation, the Participating Institutions, the National Science Foundation, the U.S. Department of Energy, the National Aeronautics and Space Administration, the Japanese Monbukagakusho, the Max Planck Society, and the Higher Education Funding Council for England. The SDSS website is http://www.sdss.org/.

The SDSS is managed by the Astrophysical Research Consortium for the Participating Institutions. The Participating Institutions are the American Museum of Natural History, the Astrophysical Institute Potsdam, the University of Basel, the University of Cambridge, Case Western Reserve University, the University of Chicago, Drexel University, Fermilab, the Institute for Advanced Study, the Japan Participation Group, Johns Hopkins University, the Joint Institute for Nuclear Astrophysics, the Kavli Institute for Particle Astrophysics and Cosmology, the Korean Scientist Group, the Chinese Academy of Sciences (LAMOST), Los Alamos National Laboratory, the Max Planck Institute for Astronomy (MPIA), the Max Planck Institute for Astrophysics (MPA), New Mexico State University, Ohio State University, the University of Pittsburgh, the University of Portsmouth, Princeton University, the United States Naval Observatory, and the University of Washington.

Funding for SDSS-III has been provided by the Alfred P. Sloan Foundation, the Participating Institutions, the National Science Foundation, and the U.S. Department of Energy Office of Science. The SDSS-III website is http://www.sdss3.org/.

SDSS-III is managed by the Astrophysical Research Consortium for the Participating Institutions of the SDSS-III Collaboration, including the University of Arizona, the Brazilian Participation Group, Brookhaven National Laboratory, Carnegie Mellon University, the University of Florida, the French Participation Group, the German Participation Group, Harvard University, the Instituto de Astrofisica de Canarias, the Michigan State/Notre Dame/JINA Participation Group, Johns Hopkins University, Lawrence Berkeley National Laboratory, the Max Planck Institute for Astrophysics, the Max Planck Institute for Extraterrestrial Physics, New Mexico State University, New York University, The Ohio State University, Pennsylvania State University, the University of Portsmouth, Princeton University, the Spanish Participation Group, the University of Tokyo, the University of Utah, Vanderbilt University, the University of Virginia, the University of Washington, and Yale University.

Software: emcee (Foreman-Mackey et al. 2013), Cloudy (Ferland et al. 2013), pymccorrelation (Privon et al. 2020), mlinmix_err (Kelly 2007), Sherpa (Freeman et al. 2001), SimBAL (Leighly et al. 2018), GMM (Muratov & Gnedin 2010).

ORCID iDs

Karen M. Leighly https://orcid.org/0000-0002-3809-0051
Hyunseop Choi https://orcid.org/0000-0002-3173-1098
Donald M. Terndrup https://orcid.org/0000-0002-0431-1645
Sarah C. Gallagher https://orcid.org/0000-0001-6217-8101
Gordon T. Richards https://orcid.org/0000-0002-1061-1804

References

Akritas, M. G., & Bershady, M. A. 1996, ApJ, 470, 706
Bailey, S. 2012, PASP, 124, 1015
Baldwin, J. A. 1977, ApJ, 214, 679
Baskin, A., Laor, A., & Hamann, F. 2015, MNRAS, 449, 1593
Bentz, M. C., Peterson, B. M., Pogge, R. W., Vestergaard, M., & Onken, C. A. 2006, ApJ, 644, 133
Bevington, P. R. 1969, Data Reduction and Error Analysis for The Physical Sciences (New York: McGraw-Hill)
Boroson, T. A. 2002, ApJ, 565, 78
Boroson, T. A., & Green, R. F. 1992, ApJS, 80, 109
Brotherton, M. S., Wills, B. J., Francis, P. J., & Steidel, C. C. 1994, ApJ, 430, 495
Choi, H., Leighly, K. M., Terndrup, D. M., et al. 2022, arXiv:2203.11964
Choi, H., Leighly, K. M., Terndrup, D. M., Gallagher, S. C., & Richards, G. T. 2020, ApJ, 891, 53
Coatman, L., Hewett, P. C., Banerji, M., et al. 2017, MNRAS, 465, 2120
Cohen, R. D. 1983, ApJ, 273, 489
Collin, S., Kawaguchi, T., Peterson, B. M., & Vestergaard, M. 2006, A&A, 456, 75
Corbin, M. R., & Boroson, T. A. 1996, ApJS, 107, 69
Dabbieri, C., Leighly, K., & Richards, G. 2020, AAS Meeting Abstracts, 236, 238.03
de Kool, M., Arav, N., Becker, R. H., et al. 2001, ApJ, 548, 609
de Kool, M., Becker, R. H., Gregg, M. D., White, R. L., & Arav, N. 2002, ApJ, 567, 58
Elvis, M. 2000, ApJ, 545, 63
Eracleous, M., Halpern, J. P., & Charlton, J. C. 2003, ApJ, 582, 633
Ferland, G. J., Porter, R. L., van Hoof, P. A. M., et al. 2013, RMxAA, 49, 137
Foreman-Mackey, D., Hogg, D. W., Lang, D., & Goodman, J. 2013, PASP, 125, 306
Francis, P. J., Hewett, P. C., Foltz, C. B., & Chaffee, F. H. 1992, ApJ, 398, 476

Frank, J., King, A., & Raine, D. J. 2002, Accretion Power in Astrophysics: Third Edition (Cambridge: Cambridge Univ. Press)
Freeman, P., Doe, S., & Siemiginowska, A. 2001, Proc. SPIE, 4477, 76
Gallagher, S. C., Richards, G. T., Lacy, M., et al. 2007, ApJ, 661, 30
Ganguly, R., Brotherton, M. S., Cales, S., et al. 2007, ApJ, 665, 990
Gibson, R. R., Jiang, L., Brandt, W. N., et al. 2009, ApJ, 692, 758
Giustini, M., & Proga, D. 2019, A&A, 630, A94
Grupe, D. 2004, AJ, 127, 1799
Hall, P. B., Anderson, S. F., Strauss, M. A., et al. 2002, ApJS, 141, 267
Halpern, J. P. 1997, in AAS Conf. Ser. 128, Mass Ejection from Active Galactic Nuclei, ed. N. Arav, I. Shlosman, & R. J. Weymann (San Francisco, CA: ASP), 41
Halpern, J. P., Eracleous, M., Filippenko, A. V., & Chen, K. 1996, ApJ, 464, 704
Hamann, F., Herbst, H., Paris, I., & Capellupo, D. 2019, MNRAS, 483, 1808
Hartigan, J. A., & Hartigan, P. M. 1985, AnSta, 13, 70
Hewett, P. C., & Foltz, C. B. 2003, AJ, 125, 1784
Hewett, P. C., Foltz, C. B., & Chaffee, F. H. 1995, AJ, 109, 1498
Isobe, T., Feigelson, E. D., Akritas, M. G., & Babu, G. J. 1990, ApJ, 364, 104
Isobe, T., Feigelson, E. D., & Nelson, P. I. 1986, ApJ, 306, 490
Jester, S., Schneider, D. P., Richards, G. T., et al. 2005, AJ, 130, 873
Kelly, B. C. 2007, ApJ, 665, 1489
Knigge, C., Scaringi, S., Goad, M. R., & Cottis, C. E. 2008, MNRAS, 386, 1426
Kovačević, J., Popović, L. Č., & Dimitrijević, M. S. 2010, ApJS, 189, 15
Krawczyk, C. M., Richards, G. T., Gallagher, S. C., et al. 2015, AJ, 149, 203
Laor, A., & Brandt, W. N. 2002, ApJ, 569, 641
Leighly, K. M. 2004, ApJ, 611, 125
Leighly, K. M., Terndrup, D. M., Gallagher, S. C., Richards, G. T., & Dietrich, M. 2018, ApJ, 866, 7
Leighly, K. M., Terndrup, D. M., Lucy, A. B., et al. 2019, ApJ, 879, 27
Ludwig, R. R., Wills, B., Greene, J. E., & Robinson, E. L. 2009, ApJ, 706, 995
Muratov, A. L., & Gnedin, O. Y. 2010, ApJ, 718, 1266
Nemmen, R. S., Georganopoulos, M., Guiriec, S., et al. 2012, Sci, 338, 1445
Osterbrock, D. E., & Ferland, G. J. 2006, Astrophysics of Gaseous Nebulae and Active Galactic Nuclei (Sausalito, CA: University Science Books)
Pâris, I., Petitjean, P., Aubourg, É., et al. 2018, A&A, 613, A51
Pâris, I., Petitjean, P., Rollinde, E., et al. 2011, A&A, 530, A50
Pâris, I., Petitjean, P., Ross, N. P., et al. 2017, A&A, 597, A79
Privon, G. C., Ricci, C., Aalto, S., et al. 2020, ApJ, 893, 149
Rankine, A. L., Hewett, P. C., Banerji, M., & Richards, G. T. 2020, MNRAS, 492, 4553
Rankine, A. L., Matthews, J. H., Hewett, P. C., et al. 2021, MNRAS, 502, 4154
Reichard, T. A., Richards, G. T., Hall, P. B., et al. 2003, AJ, 126, 2594
Runnoe, J. C., Ganguly, R., Brotherton, M. S., & DiPompeo, M. A. 2013, MNRAS, 433, 1778
Sawicki, M. 2012, PASP, 124, 1208
Schulze, A., Schramm, M., Zuo, W., et al. 2017, ApJ, 848, 104
Shang, Z., Wills, B. J., Robinson, E. L., et al. 2003, ApJ, 586, 52
Shen, Y. 2016, ApJ, 817, 55
Shen, Y., & Ho, L. C. 2014, Natur, 513, 210
Strateva, I. V., Strauss, M. A., Hao, L., et al. 2003, AJ, 126, 1720
Sulentic, J. W., Marziani, P., & Dultzin-Hacyan, D. 2000, ARA&A, 38, 521
Tolea, A., Krolik, J. H., & Tsvetanov, Z. 2002, ApJL, 578, L31
Trump, J. R., Hall, P. B., Reichard, T. A., et al. 2006, ApJS, 165, 1
Véron-Cetty, M.-P., Joly, M., & Véron, P. 2004, A&A, 417, 515
Voelker, J., Choi, H., Leighly, K., DeFrancesco, C., & Dabbieri, C. 2021, AAS Meeting Abstracts, 53, 337.10
Wang, J., Wei, J. Y., & He, X. T. 2006, ApJ, 638, 106
Weymann, R. J., Morris, S. L., Foltz, C. B., & Hewett, P. C. 1991, ApJ, 373, 23
Wills, B. J., Laor, A., Brotherton, M. S., et al. 1999, ApJL, 515, L53
Wolf, J., Salvato, M., Coffey, D., et al. 2020, MNRAS, 492, 3580
Yi, W., Brandt, W. N., Hall, P. B., et al. 2019, ApJS, 242, 28
Yip, C. W., Connolly, A. J., Vanden Berk, D. E., et al. 2004, AJ, 128, 2603
Yuan, M. J., & Wills, B. J. 2003, ApJL, 593, L11
Zakamska, N. L., & Greene, J. E. 2014, MNRAS, 442, 784